https://doi.org/10.5194/egusphere-2026-3164
Preprint. Discussion started: 23 June 2026

Robust attribution of global industrial-era glacier mass loss to anthropogenic climate change

Mira Berdahl[1], John Erich Christian[2], and Gerard H. Roe[1]

[1]Department of Earth and Space Sciences, University of Washington, Seattle, WA, USA
[2]Department of Geography, University of Oregon, Eugene, OR, USA

Correspondence: Mira Berdahl (mberdahl@uw.edu)

Abstract.

We apply formal climate-attribution methods to industrial-era glacier mass loss at both regional and individual glacier scales. Using a combination of observed temperatures and climate-model simulations, we show that warming across all glacierized regions of the globe is attributable to anthropogenic climate change. Our central estimates are that the magnitude of the anthropogenic warming over the industrial era ranges from from 91-98% of the observed, depending on region. These temperature changes equate to regional equilibrium-line-altitude (ELA) rises of 107-340 m, all of which are at least *extremely likely* anthropogenic in origin.

We examine 75 individual glaciers around the world, using realistic geometries and mass-balance profiles to reconstruct approximate preindustrial glacier geometries. Using these preindustrial geometries as reference surfaces, we analyze mass balance on these surfaces and show that anthropogenic ELA rise has produced sweeping changes in ablation and accumulation across all sampled glaciers. We find that a glacier's sensitivity to ELA rise is governed more strongly by local catchment geometry than by climatic setting. Since these industrial-era mass-balance changes are driven by the anthropogenic warming, our central estimates of the anthropogenic contribution are the same as for temperature.

Finally, we compare these anthropogenically driven changes against the distribution of natural mass-balance variability drawn from both climate-model counterfactual simulations and last-millennium reconstructions at each of our 75 glaciers. Across all glacierized regions, it is *virtually certain* the anthropogenic mass-balance signal is outside the envelope of natural variability, as characterized by both preindustrial climate reconstructions and the CMIP counterfactual ensemble. Within our analysis framework, we conclude it is *very likely* that anthropogenic warming is the *primary driver* of industrial-era mass loss.

1 Introduction

The widespread industrial-era retreat of mountain glaciers is often invoked as clear evidence of anthropogenic climate change. Side-by-side photographs of mountain glaciers taken from the same vantage point showcase stark retreats between the early twentieth century and modern-day, with the implication and commonplace understanding that the observed retreat is due to human emissions. And yet the Intergovernmental Panel on Climate Change (IPCC) makes relatively weak assertions about the connection between modern glacier retreat and anthropogenic climate change. The strongest assessment, in the most recent

https://doi.org/10.5194/egusphere-2026-3164
Preprint. Discussion started: 23 June 2026

report (Eyring et al., 2023), is that "..., we conclude that human influence is *very likely*[1] the main driver of the near-universal retreat of glaciers globally since the 1990s." If the research community's consensus is that it is only the retreat since the 1990s that can confidently be attributed to human influence, then arguably it is misleading for glacier images from the nineteenth and early twentieth century to be used in the public communication of the impacts of anthropogenic climate change. Attribution statements in prior IPCC reports are even more circumspect about the role of human activity in industrial-era retreat.

There are a few issues that have impeded a more robust attribution of glacier retreat. First, there has been uncertainty about the natural variability of glacier size. Paleoglacial records demonstrate that mountain glaciers have advanced and retreated repeatedly throughout the Holocene (Solomina et al., 2016; Grove, 2013) in response to natural forcing from solar variability, volcanism, and interannual variability due to internal climate dynamics, with no single dominant mechanism operating at a global scale (e.g., Huston et al., 2021). This natural variability is not always spatially coherent, implying that regional climate variability also plays an important role (Neukom et al., 2019).

Second, there is the possibility that recent glacier retreat is simply a delayed response from a preceding Little Ice Age (LIA). Because glacier response times are typically multidecadal, the present-day glacier position represents a mixed response to past natural climate variability, and to industrial-era anthropogenic forcing (Marzeion et al., 2018). So it is possible, for instance, that some of the early industrial-era retreat might be a natural recovery from LIA maxima. One technical issue is that most industrial-era climate-model simulations start only at 1850. If their output is used to drive glacier-length simulations, the glacier model must be initialized through a parameter-calibration procedure, rather than naturally resulting from the antecedent climate history. This initialization uncertainty can lead to an artificial model drift that adds uncertainty to the interpretation of industrial-era retreat. For example, model output in Marzeion et al. (2014a) and Clauzel et al. (2023) exhibit industrial-era drifts even under natural forcing. Finally, the problem is further complicated by the fact that the LIA itself was not a globally synchronous event (Neukom et al., 2019).

In this study, we adopt the climate-attribution methodologies that formed the basis for IPCC assessments of global temperature attribution (e.g., Hegerl et al., 2010; Gillett et al., 2013, 2021; Ribes et al., 2021; Eyring et al., 2023), and apply them to melt-season temperature attribution on regional and local glacier scales. We then convert the temperature attribution to changes in equilibrium-line altitude (ELA) and mass balance. The mass-balance analysis is based on the concept of a glacier reference surface, originally introduced to more-directly quantify the effects of climate change on glacier mass balance by removing the effects of changing glacier geometry (Elsberg et al., 2001). This measure of mass balance circumvents the need to represent glacier dynamics.

---

[1] We use IPCC attribution language throughout, defined in Table A2. Our confidence bounds are based on a two-tailed test, which is conservative. Given that the sign of change is known, a one-sided bound could be argued for.

https://doi.org/10.5194/egusphere-2026-3164
Preprint. Discussion started: 23 June 2026

Consistent with the IPCC, we find that the glacierized regions of the world have all experienced industrial-era warming that is attributable to anthropogenic climate change. The central estimates of the magnitude of the anthropogenic warming range from 91-99%, depending on region. This warming is accompanied by attributable changes of 100s of meters in ELA above the changes expected in a naturally forced world. At the local scale, we show that industrial-era warming is *very likely* to be the primary driver of the mass-balance changes at 95% of the sampled glacier locations, and that these observed changes also far exceed the natural mass-balance variability of the preceding millennium.

2 Attribution of industrial-era changes in melt-season temperature and ELA

Our approach compares observations of industrial-era changes in melt-season-temperature, with *counterfactual* climate-model simulations that omit anthropogenic forcing over the same period. The counterfactual simulations populate a distribution of the temperature changes that might have occurred from only natural forcing and internal variability. The difference between the observed signal and the counterfactual distribution yields both a central estimate of the anthropogenic fraction and a measure of the signal-to-noise ratio, which we interpret using the IPCC probability terminology (Table A2). The inclusion of a counterfactual, "what-if", analysis of what would have happened without human influence is imperative to meet the conditions that the IPCC sets for a formal attribution analysis (Hegerl et al., 2010; Bindoff et al., 2014).

For observations we use the Berkeley Earth (BE) land/ocean temperature record to assess temperature change over the industrial era. BE surface temperatures are available from 1850-2024 as a gridded global product on a 1x1° grid (Rohde and Hausfather, 2020). BE provides a spatially complete and homogenous temperature field, and its global-mean temperature records are comparable to other products such as NASA's GISSTEMP, NOAA's GlobalTemp and Hadley's HadCRUT4 (Rohde and Hausfather, 2020). Data coverage can be poor early in the record, particularly in the Southern Hemisphere, but becomes reasonably comprehensive after 1875. In computing regional-mean climatologies, missing data are excluded, and we aim for a minimum of 30 years of valid data.

For the counterfactual climates, we use natural-forcing-only global-climate-model (GCM) simulations (so-called “hist-nat") from the coupled model intercomparison projects, CMIP5 (Taylor et al., 2012) and CMIP6 (Eyring et al., 2016), run as part of the Diagnostic, Evaluation and Characterization of Klima (DECK) standard simulations. These simulations, totaling 205 ensemble members, include all natural forcings such as orbital, aerosol and volcanic sources. They can alternatively be described as "all-but-anthropogenic" forcing simulations. More details on the simulations used in this study can be found in Appendix A.

In this study we focus on melt-season temperature, and do not consider changes in precipitation. Observed trends in mean-annual precipitation are generally small and statistically insignificant (Masson-Delmotte et al., 2021), consistent with expectations from thermodynamic constraints and climate-model output (Allen and Ingram, 2002; Held and Soden, 2006; Atwood et al., 2021). The impact of temperature on the partitioning of precipitation into rain versus snow is included in the vertical mass-balance profiles that we use in Section 3. Further analyses supporting the predominant importance of temperature trends over precipitation trends for mass-balance trends are provided in Marzeion et al. (2014b) and Roe et al. (2021). We define summer melt season as June–July–August–September (JJAS) at latitudes $> 30°$N, December-January-February–March (DJFM) for $> 30°$S and annual means between 30°S and 30°N.

2.1 Case study for Argentière glacier, France

We begin with the example of Argentière Glacier, a well-studied glacier located in the Mont-Blanc massif in the French Alps. Historical length measurements at Argentière extend back to the year 1600, while modern observations using stake measurements, geodetic surveys, GPS and ground-penetrating radar have produced a detailed characterization of glacier geometry and dynamics. Argentière has therefore been the subject of numerous glaciological and attribution studies (e.g., Huybrechts et al., 1989; Rabatel et al., 2018; Protin et al., 2019; Clauzel et al., 2023).

We show melt-season temperature at Argentière relative to an early industrial-era baseline (1850-1905)[2] in Figure 1a. We define the industrial-era change as the difference between the most recent 15 years of the record (2010-2024) and the mean temperature of the baseline period. We use this shorter, 15-yr, recent period rather than the conventional 30-year window to more faithfully capture the significant acceleration of global warming since around 2015 (Foster and Rahmstorf, 2026). More details on this choice can be found in Section 3.2. By this measure, Argentière has experienced an industrial-era warming of 1.98 °C (Figure 1b).

The distribution of industrial-era temperature changes from natural-only forcing is constructed from the $\sim$200 hist-nat ensemble members (Appendix Table A1). Unlike the observed record, the natural simulations show no evidence of a recent warming trend, so we compute industrial-era temperature changes as the difference between the preindustrial baseline and the final available 30-year climatology in each simulation. A 30-year average provides a more stable and representative estimate of the natural climate state than a shorter window would. This ensemble forms a distribution of the counterfactual changes in climatology that might have occurred without human forcing of climate (Fig 1b). The mean and standard deviation of this distribution are -0.0006°C and 0.20°C, respectively.

The observed industrial-era warming sits far outside the counterfactual envelope (Fig. 1b). We define the central estimate of the attributable warming as the difference between the observed warming signal ($\mathrm{T_{obs}}$) and the mean of the naturally forced distribution of industrial-era trends (μ_{nat}), such that $\Delta \mathrm{T} = \mathrm{T_{obs}} - \mu_{\mathrm{nat}}$. Then, consistent with IPCC language, we take the *likely* range of the attributable warming as the $\pm 1\sigma$ width of the naturally forced distribution of industrial-era trends (σ_{T}). In the case of Argentière this yields an attributable warming of $1.98 \pm 0.20°$ C. Expressed as a percentage this is $100 \pm 10.2\%$ of

---

[2] The early-industrial baseline extends to 1905 rather than 1900 to capture at least 30 years of valid data, since BE coverage is sparse in many locations prior to 1875.

the observed warming. We note that the attributable anthropogenic warming may exceed 100% of the observed if the counterfactual (naturally forced) climate would have otherwise been cooling. We can also characterize this in terms of a signal-to-noise ratio (SNR), where $\mathrm{SNR} = \Delta \mathrm{T}/\sigma_\mathrm{T}$. A $\mathrm{SNR} > 2$ indicates that the observed warming is more than twice the standard deviation of the distribution of natural industrial-era trends, corresponding to the IPCC threshold as '*extremely likely*' outside the bounds of natural variability. At Argentière, the temperature SNR equals 9.9, placing the attribution as '*virtually certain*'.

An important point, visually clear in Figure 1, is that while our attribution applies to the full industrial-era period, that is not the same thing as saying anthropogenic warming exceeded natural variability at every moment in the industrial era. While anthropogenic forcing was certainly creating an underlying warming tendency, it is perfectly consistent to say that the magnitude of that warming did not rise outside the envelope of variability until later in the twentieth century. If the target is cumulative human influence on the cryosphere, then the full industrial era is the correct attribution interval to pick. It is speculation on our part, but it may be that the surprisingly late date in the IPCC AR6 report of "*since the 1990s*" (Eyring et al., 2023) may have been influenced by this distinction.

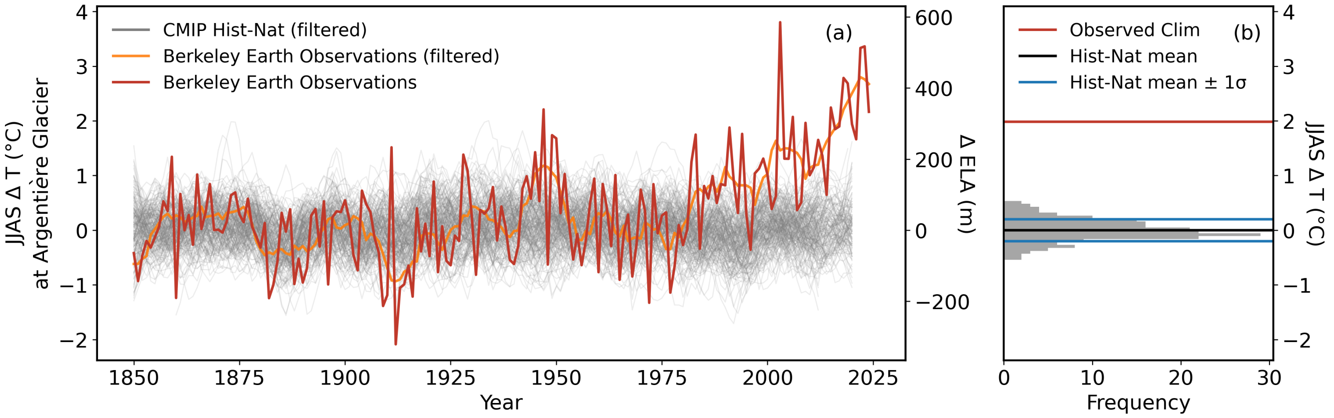

Figure 1. (a) Summertime temperature histories at Argentière Glacier, France. Summer melt-season (JJAS) industrial-era temperature anomalies from Berkeley Earth observations (red), and CMIP5 and CMIP6 hist-nat counterfactual simulations (grey spaghetti curves). For visualization purposes only, the hist-nat simulations have been filtered using a Savgol low-pass filter, with the analagous filter applied to the BerkeleyEarth data in reverse (orange). Secondary y-axis shows corresponding changes in ELA assuming a fixed 6.5 $^\circ\mathrm{C\,km^{-1}}$ lapse rate. (b) A summary of industrial-era temperature changes, computed as the difference between the 1850-1905 early PI climate and the most recent 15 years of the observational (Berkeley Earth) data. The grey distribution shows the hist-nat industrial-era climate ensemble, with the mean and standard deviations of the natural variability in black and blue lines, respectively. The observed temperature change at this location (1.98°C) is shown with the red line, well outside the range of variability of the counterfactual simulations.

https://doi.org/10.5194/egusphere-2026-3164
Preprint. Discussion started: 23 June 2026

2.2 Extension to all glacierized regions

We extend the same methodology used on Argentière to the full set of global glacierized regions. Using every ice-containing grid cell in each RGI region, we compute the area-weighted regional mean temperature for both the observed climate ($\mathrm{T_{obs}}$) and for each counterfactual ensemble member. Regional attribution statistics are then computed as the difference between the observed regional mean and the ensemble mean of the counterfactual regional climates ($\Delta\mathrm{T}$), with uncertainty (σ_T) derived from the standard deviation of the 205 counterfactual regional values. Across all 19 glacierized regions examined, central estimates of the anthropogenic fraction of observed warming range from 90–99%, with a global mean (excluding Antarctica) of 94% (likely range 80–108%) (Table 1 & Fig. 2a, where dot color describes the magnitude of $\Delta\mathrm{T}$ and dot area scales with SNR). For 16 of 19 regions, signal-to-noise ratios exceed 3 (∼99-100% probability). In other words, under the IPCC terminology, it is *virtually certain* that the observed industrial-era warming cannot be due to natural variability (as defined in Appendix Table A2). For Iceland (SNR = 2.08), Svalbard (SNR = 2.60), and the Russian Arctic (SNR = 2.81) the assessment is *extremely likely*. Even the Antarctic & Subantarctic region (SNR = 3.02) is in the *virtually certain* category, with its central attributable estimate remaining above 90% even though we were constrained to use a more recent base period (1960-1990), which one would otherwise expect to result in a weaker signal. Notably, the low latitudes yield the largest temperature SNR (13.07), despite a moderate temperature change signal (1.41°C). This reflects the expected lower interannual variability in the tropics, as well as our use of annual-mean temperatures for this region (30°S to 30°N). This inflates the SNR relative to what a seasonal mean would produce.

We can convert the attributable $\Delta\mathrm{T}$ in Figure 2a to $\Delta\mathrm{ELA}$ using a melt-season lapse rate ($\equiv \Gamma$). Rather than applying a uniform 6.5° C km^{-1}, we calculate a spatially variable Γ. We derive this field from ERA5 1/4° resolution reanalysis data spanning 1979-2021 (Hersbach et al., 2020), using the same definitions for melt-season as for $\Delta\mathrm{T}$. To avoid complications from pressure levels intersecting high-level terrain, we calculate Γ between the surface (2m) and the 400 mb level, resulting in a range of values $3.5°\mathrm{C\ km}^{-1} < \Gamma < 8.1°\mathrm{C\ km}^{-1}$. We apply the relation $\Delta\mathrm{ELA} = \Delta T/\Gamma$ to produce a regional ELA attribution (Fig. 2b). From this analysis we conclude there are attributable changes of 100's of meters in ELA larger than the expected changes in a naturally forced world. Regional $\Delta\mathrm{ELA}$ values range from 107 m in the Antarctic & Subantarctic to 340 m in Northern Arctic Canada, with the strongest and most statistically robust signals found in Central Europe ($\Delta\mathrm{ELA} = 328$m, $\mathrm{SNR} = 8.4$) and the Caucasus & Middle East ($\Delta\mathrm{ELA} = 312$ m, $\mathrm{SNR} = 9.4$). Again, the high SNR in the Low Latitudes reflects the low natural climate variability at tropical latitudes rather than an unusually large signal. Observations of ELA trends are hampered by the short duration and large interannual variability in most records, but published records of recent trends are similar to our estimates where they overlap (e.g., Ohmura and Boettcher, 2022; Larocca et al., 2024; Rabatel et al., 2013). We note that while our estimated $\Delta\mathrm{ELA}$ depends on Γ, the SNR does not.

https://doi.org/10.5194/egusphere-2026-3164
Preprint. Discussion started: 23 June 2026

Region	T_{obs} (°C)	ΔT (°C)	σ_T (°C)	SNR	Central (%)	Likely Low (%)	Likely High (%)
Antarctic & Subantarctic	0.61	0.56	0.19	3.0	91.8	61.4	122.3
South Asia (West)	0.99	0.92	0.25	3.7	92.4	67.2	117.7
Iceland	1.05	0.96	0.46	2.1	91.4	47.5	135.3
Alaska	1.17	1.11	0.28	4.0	94.4	70.7	118.1
Russian Arctic	1.20	1.11	0.40	2.8	92.7	59.7	125.6
Greenland Periphery	1.23	1.15	0.26	4.4	93.4	72.1	114.6
Central Asia	1.27	1.19	0.18	6.5	93.9	79.4	108.4
Svalbard	1.33	1.20	0.46	2.6	90.2	55.4	124.9
Arctic Canada South	1.28	1.21	0.33	3.7	94.1	68.6	119.7
Southern Andes	1.28	1.23	0.14	8.5	95.7	84.4	107.0
New Zealand	1.26	1.24	0.23	5.3	98.6	80.1	117.1
South Asia (East)	1.34	1.27	0.16	8.2	94.6	83.0	106.1
Western Canada & US	1.42	1.32	0.21	6.3	93.2	78.5	108.0
Low Latitudes	1.41	1.35	0.10	13.1	95.6	88.3	103.0
Scandinavia	1.44	1.35	0.33	4.1	93.9	70.9	117.0
North Asia	1.42	1.36	0.19	7.3	95.8	82.7	108.9
Arctic Canada North	1.52	1.45	0.28	5.2	95.3	77.0	113.5
Caucasus & Middle East	2.08	2.00	0.21	9.4	95.9	85.7	106.1
Central Europe	2.06	2.02	0.24	8.4	98.0	86.3	109.8
Global Mean (excluding Antarctica)	1.28	1.20	0.18	6.8	93.9	80.1	107.7

Table 1. Regional attribution summary for temperature change, ranked in ascending order of ΔT. All regional values are area-weighted by grid cell size and computed with respect to the 1850-1905 baseline period. T_{obs} refers to the observed signal of modern (2010-2024) climate, ΔT is the difference in this signal from the counterfactual (Gaussian) mean ($T_{obs} - \mu_T$), σ_T is one standard deviation (also based on a Gaussian distribution), SNR is signal-to-noise ratio ($\Delta T/\sigma_T$), and the central and likely estimates refer to the attributable portion of the signal. We note that the attributable anthropogenic warming may exceed 100% of the observed if the counterfactual (naturally forced) climate would have otherwise been cooling. Global mean excludes Antarctica, whose baseline climatology is shorter than the rest of the regions due to a lack of data before 1956.

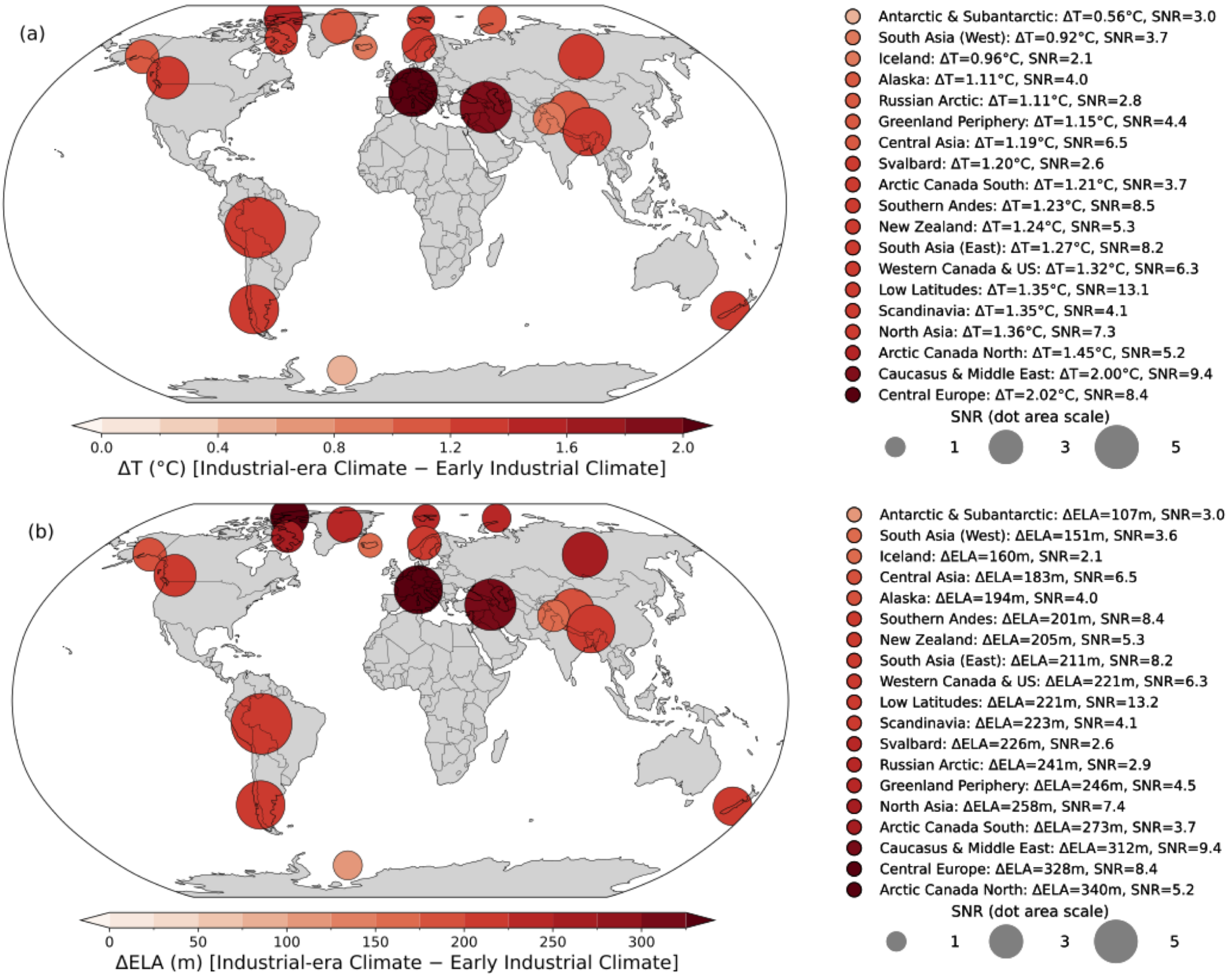

Figure 2. (a) Attributable ΔT, for each RGI region. ΔT is computed as the difference between the observed industrial-era (2010-2014) climate and the mean of the distribution of the counterfactual industrial-era (most recent 30 years available) ensemble. Colors correspond to the ΔT magnitude, and the circle area is scaled by SNR magnitude. Captions ranked in ascending order of ΔT. Dots are computed for, and centered on, RGI6 regions. Antarctica and Greenland include only peripheral glaciers, excluding the ice sheet portion. (b) ΔELA, converted from ΔT using the a lower free troposphere (surface-400mb) lapse rate, Γ: $\Delta\text{ELA} = \Delta T/\Gamma$. See text for details.

.

3 Application to mass-balance changes

The attributable warming and the resultant ELA changes are useful metrics of anthropogenic climate change at the local scale, but it is also important to quantify the impact of those changes on glacier mass balance, which reflects how the glacier geometry experiences these local climate changes. In order to do that, we adopt Elsberg et al. (2001)'s concept of a *reference surface* for a glacier, which was originally introduced to connect observations of glacier mass balance more directly to climate. Elsberg et al. (2001) pointed out that observations are made on a glacier surface that is itself evolving, so standard mass-balance records reflect a climate signal that is convolved with the glacier dynamics. By instead estimating mass balance on a fixed, reference glacier surface, they were able to create a more direct evaluation of the impact of climate change. Paul (2010) estimated that, for 60 glaciers in the Alps, only 30-50% of the glacier "reaction" to climate change is reflected in conventional mass-balance records, with the rest being "hidden" by the geometric adjustment (both area and thickness). Other research has used the concept of a reference surface (e.g., Harrison et al., 2005; Huss et al., 2012), noting that reference-surface mass balances are well-suited for climatic interpretations (e.g., Cogley et al., 2011).

It is important to note that the reference-surface mass balance is distinct from the actual glacier mass balance (sometimes termed the *conventional* mass balance). It is also not the cumulative mass loss over the industrial era. However, it has several advantages as a variable for attribution assessments. First, the reference-surface concept allows us to apply our temperature-attribution results to more glacier-relevant metrics in a way that does not require modeling the glacier dynamics. Using reference surfaces allows us to circumvent the initial-condition uncertainty that arises in a transient numerical simulation starting, for example, in 1850. Our method does not require an exact match to the transient history of the specific glacier, since the impacts of past, observed, and counterfactual industrial-era climates are all evaluated on the same fixed surface. Second, the SNR of reference-surface mass balance is more directly relatable to that of temperature and ELA, whereas the SNR for the mass balance of an evolving glacier geometry is affected by the buffering of the glacier dynamics. Consider the limiting case of a slowly-evolving climate change or, equivalently, a fast glacier response time, where the glacier retreat keeps pace in quasi-equilibrium with the forcing. In such a situation, the SNR of mass balance would remain low even as the forcing and its cumulative effects grow. The degree to which current mass balance exceeds natural variability is thus dependent on the recent rate of forcing and the glacier's response timescale, making it a more complex variable for attribution. An analogous case would be the planet's instantaneous radiative imbalance, which is due to anthropogenic forcing but also damped by the planet's warming, compared to the effective radiative forcing (ERF) which is evaluated for a fixed surface temperature (Forster et al., 2021). The ERF framework allows for a clean separation of different global radiative-forcing components. In our case, the reference-surface mass balance cleanly highlights the difference between modern and preindustrial climates for a given glacier.

For each glacier that we analyze, we define the reference surface as the estimated glacier surface in the mid-nineteenth century at the start of the industrial era, or what is often (but not always) called the end of the Little Ice Age (LIA). In other words, the reference surface is a counterfactual glacier in the same way that the hist-nat simulations are a counterfactual climate. This choice means that applying the attributable warming to the reference surface yields an industrial-era mass-balance change to compare with the hist-nat mass balances in the signal-to-noise framework. It is also the natural reference surface to evaluate the impact of preindustrial temperature variability estimated from paleoclimate reconstructions. We first present our method-

https://doi.org/10.5194/egusphere-2026-3164
Preprint. Discussion started: 23 June 2026

ology applied to Argentière glacier as a case study, and then extend the analysis to a globally-distributed network of 75 glaciers.

3.1 Case study for Argentière glacier, France

The Open Global Glacier Model (OGGM, Maussion et al., 2019) provides a database for the geometry of any glacier in the Randolph Glacier Inventory (RGI). We extract the bed geometry and valley width along the central flowline for Argentière, using the OGGM elevation-band method (Fig. 3a,b). We also use the OGGM calibrated mass-balance scheme. This scheme is based on the observed monthly climatology, contains an orographic-precipitation enhancement factor, a temperature-dependent rain/snow condition, and a temperature index method for calculating melt (Marzeion et al., 2012). It is calibrated according to the procedure described in Maussion et al. (2019). Climate changes are implemented in this scheme by adding a temperature offset equal to the attributable melt-season-temperature perturbation. This temperature offset changes both the melting and the rain-snow condition. We experimented with changing each monthly temperature separately but obtained similar results when implementing the melt-season temperature change uniformly.

We will refer to the glacier position at around 1850 as the Little-Ice-Age (LIA) length. For Argentière, we determine this from the dataset of Leclercq et al. (2014). The LIA terminus was approximately 1700 m further down-valley than the 2010[3] location. To obtain a glacier surface consistent with this length we use a 1.5D shallow-ice flowline model from Roe (2011) (and use the same parameters), in turn based on Oerlemans (1986). It is termed 1.5D because the ice flux accounts for changes in valley width, but the shear stresses are determined only by the thickness and slope of the flowline. The temperature offset parameter in the mass-balance scheme is incrementally adjusted until the glacier profile matches the estimated LIA position. This gives us a baseline case of a glacier surface (Fig. 3a) and a vertical profile of mass balance (Fig. 3c) that are in steady-state balance with each other. This glacier surface becomes our fixed reference surface on which we evaluate the mass-balance consequences of anthropogenically-driven temperature change.

Let $b(x)$ be the mass balance (in $\mathrm{m\ yr^{-1}}$) as a function of distance from the head of the glacier, x; let $w(x)$ be the contributing catchment width at x, and let z represent elevation above sea level. The left-hand axis (blue line) of Fig. 3d plots the product $b(x)w(x)$, which is the net mass input per unit length along the flowline (in $\mathrm{m^2\ yr^{-1}}$). It is positive in the accumulation zone, and it is large where the contributing valley width is large (cf. Fig. 3b, 3d). The baseline curve (solid blue) crosses zero at the ELA, which occurs at $x \simeq 2.8\ \mathrm{km}$ from the glacier head (Fig. 3d, blue square), $z \simeq 2680\ \mathrm{m}$ (Fig. 3c). The curve is negative in the ablation zone, but with relatively small absolute values due to the narrower valley width, until near the terminus where the mass-balance rates become increasingly negative at lower elevations (Fig. 3c, d). The right-hand axes of Fig. 3d shows the cumulative mass balance integrated along the flowline (orange line, in $\mathrm{m^3\ yr^{-1}}$). In the baseline case (solid orange), cumulative mass balance initially rises steeply within the accumulation zone, then increases more slowly as the valley narrows, before reaching a maximum at the ELA (Fig. 3d, orange square); it then declines fairly uniformly through the ablation zone,

---

[3] Clauzel et al. (2023) similarly determined a ~ 1700 m retreat since 1850 in the year 2014 based on Leclercq et al. (2014) and Protin et al. (2019)

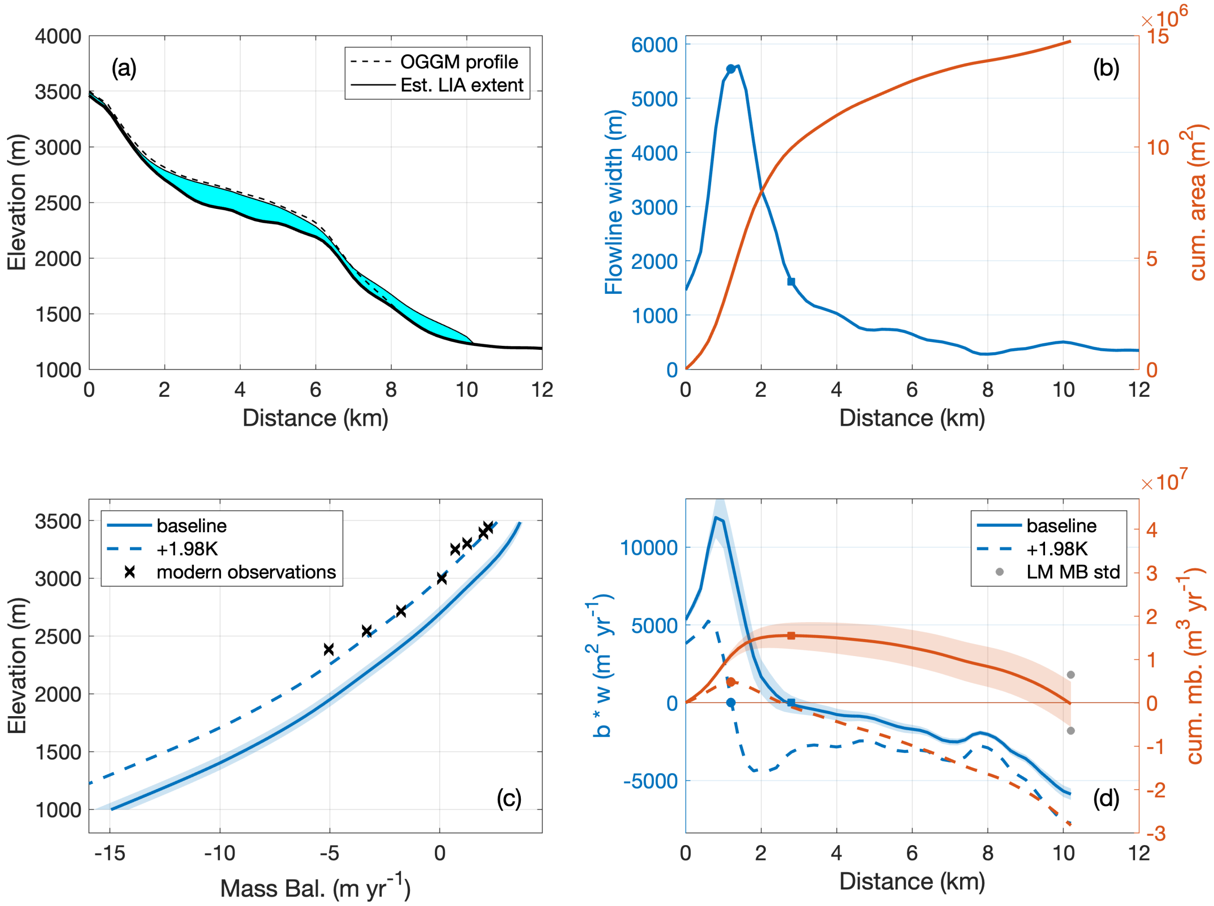

Figure 3. Industrial-era Argentière mass-balance changes over a fixed glacier reference surface. Shown are (a) Argentière modern and reference surface profiles, (b) glacier width (blue curve) and cumulative area (orange curve), (c) preindustrial (solid) and industrial-era (dashed) vertical mass-balance profile, and (d) width-integrated mass balance ($\mathrm{m}^2\mathrm{yr}^{-1}$, left axis, blue) and cumulative mass balance for baseline (right axis, red) for LIA (solid) and warmed (dashed) climates. Shaded regions in (c) and (d) represent $\pm 2\sigma$ (95% confidence) derived from the climatological analysis. Black x markers in (c) indicate industrial-era observed mass-balance measurements (2000-2019 mean) from GlacioCLIM (https://glacioclim.osug.fr). The cumulative mass balance in (d) reaches equilibrium (zero) at the terminus under baseline conditions (solid), but becomes increasingly negative under warming, indicating mass loss along almost the entire flowline. Orange square and circles in (d) indicate the ELA in the baseline and warmed climate, respectively, locations also indicated along the flowline width in panel (b). Blue square and circle in (d) indicate ELA location in the baseline and warming configurations. Grey dots in (d) indicate variability (2σ) based on last-millennium reconstruction (LMR-Seasonal).

before reaching zero at the glacier terminus, which it necessarily must do for the reference surface to represent an equilibrium profile. For the particular hypsometry of this catchment, and for this baseline case, the accumulation zone is approximately $10 \times 10^6\ \mathrm{m}^2$ of a total area of $14.7 \times 10^6\ \mathrm{m}^2$, and approximately 2.8 km (Fig. 3b, blue square) of a total flowline length of

https://doi.org/10.5194/egusphere-2026-3164
Preprint. Discussion started: 23 June 2026

10.2 km.

The impact of anthropogenic climate change is calculated by adding the local attributable industrial-era warming of 1.98 °C (Fig. 1b) to the temperature offset in the mass-balance scheme. The new mass-balance profile has an unchanged shape, but the ELA is raised by 305 m (Fig 3c). Modern (2000-2019) observations of Argentière mass balance from GLACIOCLIM (available at https://glacioclim.osug.fr, black crosses in Fig.3c) are in good agreement with the new profile. This is nice support for both the OGGM mass-balance scheme, and also for our estimated preindustrial and modern climates.

When the new mass-balance profile is applied to the reference surface, there is a dramatic impact on mass balance (dashed lines, Fig. 3d). The rise in ELA means that the accumulation area is more than halved, and mass-balance rates at any given elevation are lowered. The combination of these two factors reduces the total accumulation input by approximately 70%, from $1.55\times10^7\ \mathrm{m}^3\ \mathrm{yr}^{-1}$ to $0.48\times10^7\ \mathrm{m}^3\ \mathrm{yr}^{-1}$. Expressed as a ratio, $\mathrm{Acc}_{\mathrm{now}}/\mathrm{Acc}_{\mathrm{LIA}} = 0.31$. In contrast, the ablation area doubles, and local ablation rates increase at any given elevation. Total ablation more than doubles from $1.58\times10^7\ \mathrm{m}^3\ \mathrm{yr}^{-1}$ to $3.30\times10^7\ \mathrm{m}^3\ \mathrm{yr}^{-1}$. Expressed as a ratio, $\mathrm{Abl}_{\mathrm{now}}/\mathrm{Abl}_{\mathrm{LIA}} = 2.1$. In the warming scenario, the cumulative mass balance reaches approximately $-2.8\times10^7\mathrm{m}^3\mathrm{yr}^{-1}$, equivalent to about $-1.9\ \mathrm{m\ yr}^{-1}$ when normalized by the area. The accumulation and ablation ratios computed for Argentière ($\mathrm{Acc}_{\mathrm{now}}/\mathrm{Acc}_{\mathrm{LIA}}$ and $\mathrm{Abl}_{\mathrm{now}}/\mathrm{Abl}_{\mathrm{LIA}}$) serve as scaling factors that may be used to characterize how each component of the mass balance on the glacier surface is impacted by industrial-era warming.

It is noteworthy that, for this catchment, the reduction in accumulation is more consequential than the increase in ablation. The reason is that, at Argentière, the increase in ELA occurs across a sector of the glacier where the valley width is at a maximum (Fig. 3b). The rising ELA dramatically reduces the accumulation area (Fig. 3b, shift from blue square to circle). Moreover, even though ablation rates are relatively low just below the ELA, the large gain in ablation area in this wide sector is sufficient to drive a substantial increase in total ablation (Fig. 3d). In fact, more than half of the total cumulative mass loss in the warm scenario occurs in the first 2.5 km of the glacier's length (Fig. 6b). The effect of climate change on glacier mass balance is a complex interaction between the vertical mass-balance profile and the hypsometry of each glacier catchment. Two lessons are that mass-balance changes can happen surprisingly high in the glacier catchment, and that a wide range of catchment geometries can be expected to produce a wide range of mass-balance impacts.

The mass-balance response due to anthropogenic warming at Argentière lies far outside the range of natural variability represented by the industrial-era counterfactual simulations. In section 2.1 we found that the *likely* range of industrial-era trends under natural forcing only was ±0.20 °C. The shaded bounds in Fig. 3c,d translate this temperature uncertainty into mass-balance uncertainty, showing the *extremely likely* ($\pm2\sigma = \pm0.40$°C) range. Let σ_{mb} be the standard deviation of this range, and we can then characterize an industrial-era mass-balance signal-to-noise ratio for Argentière: $\mathrm{SNR}_{\mathrm{mb}} = |\Delta\mathrm{mb}/\sigma_{\mathrm{mb}}| = 9.9$. The bottom line for this catchment is that, with accumulation reduced by two thirds and ablation doubled, the LIA reference glacier simply cannot exist in the modern environment that our central estimate attributes entirely to anthropogenic climate change.

3.2 Extension to a globally-distributed network of glaciers

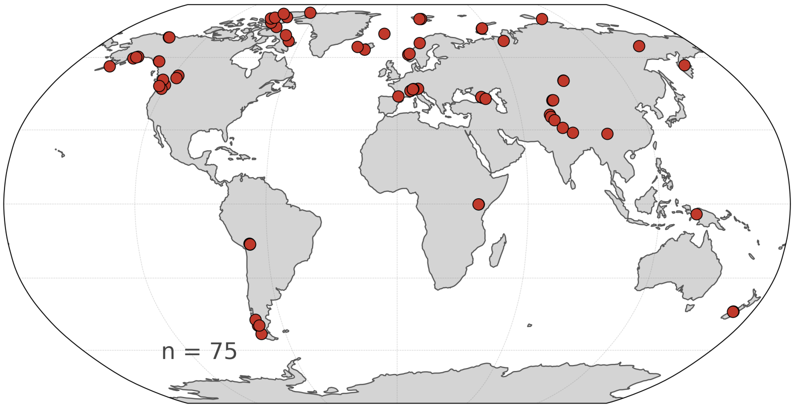

Figure 4. Map of glacier sampling locations, totaling 75 locations, sampled across all RGI regions, excluding Antarctica and Greenland. Detailed information on glacier RGI IDs and locations can be found in Table A3.

We extend this methodology to 75 global glaciers, sampling all RGI regions (excluding Antarctica and Greenland, Fig. 4), using the NASA GLIMS Viewer to identify specific glaciers and RGI IDs (GLIMS and NSIDC, 2005). We prioritize glaciers whose records extend back to or before 1850. Where available, ΔL is taken directly from the Leclercq et al. (2014) observations. Where Leclercq et al. (2014) records begin after 1850, we estimate the circa-1850 extent using a backward-extrapolated saturating exponential fit to the earliest observations, assuming glacier length approaches a quasi-equilibrium preindustrial state backward in time. Given that Leclercq et al. (2014) tends to include more well-observed regions, preindustrial length records are not available for regions such as the Canadian and Russian Arctic. To ensure sampling in each RGI region, we supplement with ΔL estimates drawn from other literature sources or, where no records exist, from reasonable assumptions of length changes for that region (detailed in the Appendix). We note that the LIA extent is not meant to precisely reconstruct the 1850 terminus position, but rather to establish a reference glacier geometry that would have been in approximate equilibrium with the cooler preindustrial climate, providing a consistent baseline against which to measure the anthropogenic signal.

Individual glacier metadata can be found in Table A3, which reports ΔT computed using a 15-year observational window (2010–2024). As a sensitivity test, we compute ΔT using a conventional 30-year window (1995-2024) on the BE data, finding a reduction in the mean attributable warming across our global glacier network by 0.32°C. This difference reflects the pronounced recent acceleration in global warming (Foster and Rahmstorf, 2026; Jenkins et al., 2022; Minière et al., 2023), which the 15-yr window is better suited to capture. Had we used an even shorter, 8-yr window (2017 to 2024), the average ΔT would have risen by 0.2 °C.

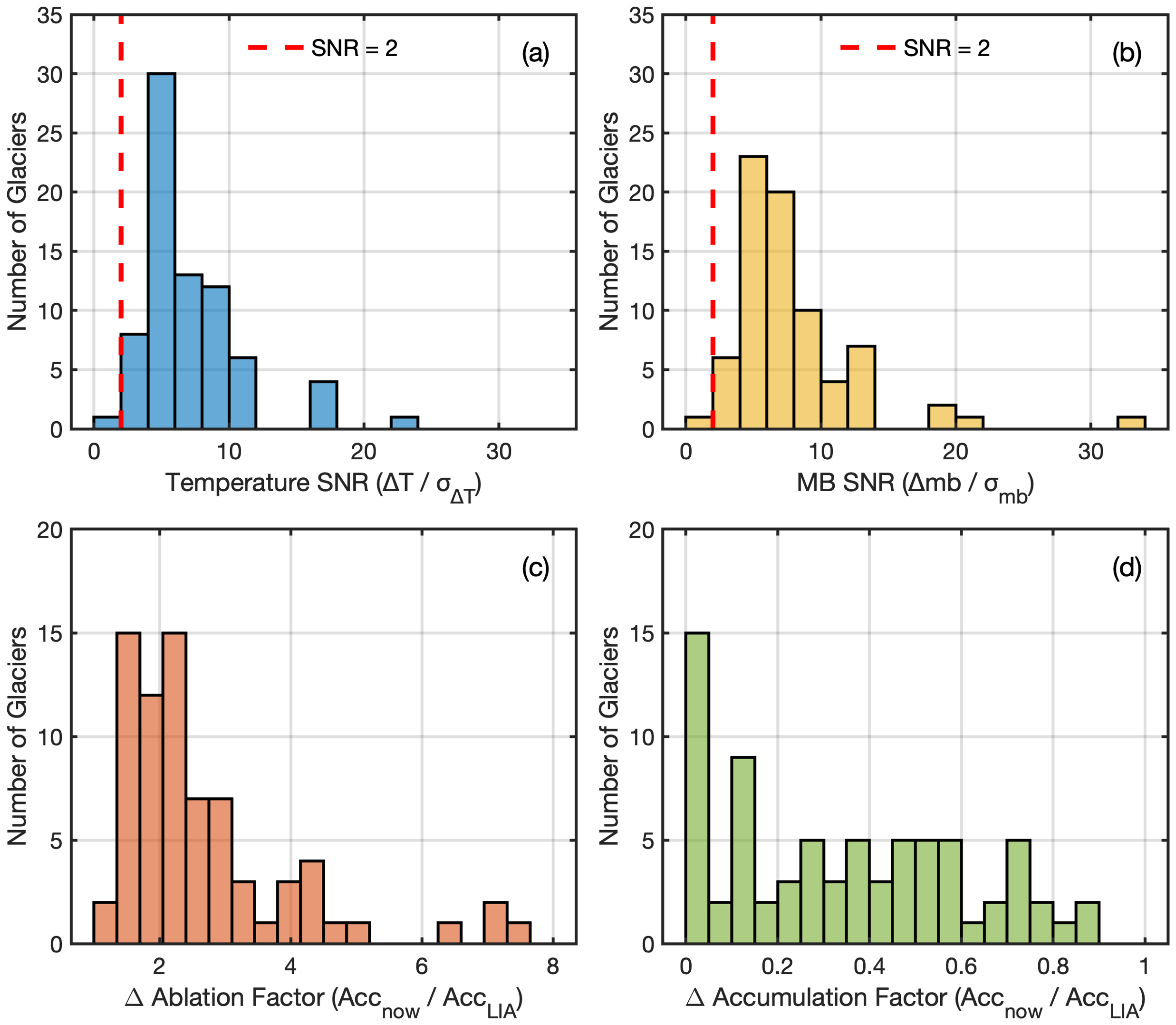

Figure 5. Mass balance results for 75 global glaciers. Distribution of (a) temperature signal-to-noise ratio ($\mathrm{SNR} = |\Delta\mathrm{T}/\sigma_\mathrm{T}|$), with dashed line at $\mathrm{SNR} = 2$, the IPCC's 'extremely likely' attribution threshold; (b) same as (a) but for reference-surface mass balance; (c) ablation ratio (Abl_{new}/Abl_{old}); and (d) accumulation ratio (Acc_{new}/Acc_{old}) across 75 glaciers. Values in (c) and (d) are the factors by which reference-surface accumulation and ablation have changed between the warmed and baseline climate states.

Across all 75 glaciers sampled, we find that anthropogenic warming produces a robust signal that drives substantial increases in ablation and losses in accumulation. The individual temperature and mass-balance signal-to-noise ratios (SNRs) at each site are calculated as the absolute anthropogenic temperature and mass-balance change ($\Delta\mathrm{T}$, $\Delta\mathrm{mb}$) divided by the standard deviation of the natural temperature and mass-balance variability ($\sigma_\mathrm{T}, \sigma_\mathrm{mb}$). They show nearly all sites (74/75) exceed the IPCC's criteria for it being '*extremely likely*' that these industrial-era reference-profile mass-balance changes are outside the bounds of natural variability), with $\mathrm{SNR} > 2$ (Fig. 5a,b). The single exception, Hyrningsjokull (Iceland), falls shy of this with a temperature and mass-balance SNR of 1.85 and 1.93 respectively, though it remains firmly in the '*very likely*' category. This slightly weaker result is due to the fairly moderate attributable temperature change ($\Delta\mathrm{T} = 0.76°$ C) and large local natural variability ($\sigma = 0.41°$ C), making the anthropogenic signal harder to distinguish from the natural fluctuations.

We can use our SNR calculations to estimate the fractional anthropogenic contribution to mass loss (Figure A1). Consistent with our warming assessment, our central estimate of the anthropogenic fraction is 101%, averaged across our network. Accounting for uncertainty ranges, and mirroring IPCC language, we define *primary driver* to mean that the fractional contribution exceeds 50%. Across our network, for 71 out of 75 glaciers it is *very likely* that anthropogenic warming is the *primary driver* of mass loss, with most having a lower bound on the *very likely* range much greater than 50%. Averaged over all glaciers in our network, it is *very likely* that the fractional anthropogenic contribution exceeds 75%.

The change in net ablation between the warmed and baseline climate states, characterized by the ablation ratio ($\mathrm{Abl}_{\mathrm{new}}/\mathrm{Abl}_{\mathrm{old}}$, where values > 1 indicate increased ablation under warming), indicates that roughly two thirds of the sampled population experiences at least a doubling of ablation under warming (Fig. 5c). Meanwhile, accumulation decreases by more than half for more than two thirds of the sampled population (Fig. 5d). The coherent, worldwide increase in ablation, and reduction in accumulation, across all sampled sites points to a pervasive climate change, global in scale, far outside the range of natural variability. Across our sample of glaciers ablation increases by a factor of 1.3 to 7.6, with a median of 2.3; and accumulation decreases to 0 to 0.9 of its preindustrial value, with a median of 0.3. These wide ranges reflect the wide variety of glacier geometries, but it is clear that preindustrial glacier geometries are completely unsustainable under industrial-era warming.

We evaluate our network for where the mass-balance changes are occurring along the reference glacier surfaces. We compile the cumulative mass imbalance for all 75 glaciers in Figure 6a, plotted against the normalized distance along the glacier centerline. A variety of different shapes can be seen, reflecting differences in the magnitude of local warming, the shape of the mass-balance gradients, and the local geometry at each site. The total mass imbalance at the terminus ranges from about -0.2 to -3 m yr^{-1} with a median of about -1 m yr^{-1}.

By further normalizing the mass imbalance as a fractional contribution, we can identify the point along the glacier length at which the curve crosses the 50% line (Fig. 6b), marking where half of the glacier's total mass loss has already occurred. For our 75 glaciers, this threshold occurs anywhere from 20% to 70% along the normalized glacier length, with a median of 35%, and depends on the interaction between the anthropogenic ELA rise and each glacier's individual hypsometry. We find it noteworthy that for 88% of our glaciers, more than half of the impact of warming on the mass balance occurs in the upper half of the reference glacier, rather than being concentrated near the terminus as might have been expected. Glaciers where the rising ELA enters a wide upper-catchment area experience a significant loss of accumulation area high up on the glacier, producing a steep early drop in the fractional profile. This type of behavior is apparent at Argentière, where large mass loss occurs in the upper reaches of the catchment (Fig. 6, red curve). Glaciers with a narrow upper basin exhibit very weak mass-balance changes in their upper reaches, but eventually show strong mass imbalance where the ELA may reach the widest sections of the glacier. This type of behavior is seen at Bolivia's Zongo glacier (Fig. 6, orange curve). Despite these nuanced responses at the individual level, every glacier we sample in this study experiences unambiguous and substantial mass loss under industrial-era warming, irrespective of local geometry and regional climate. 340

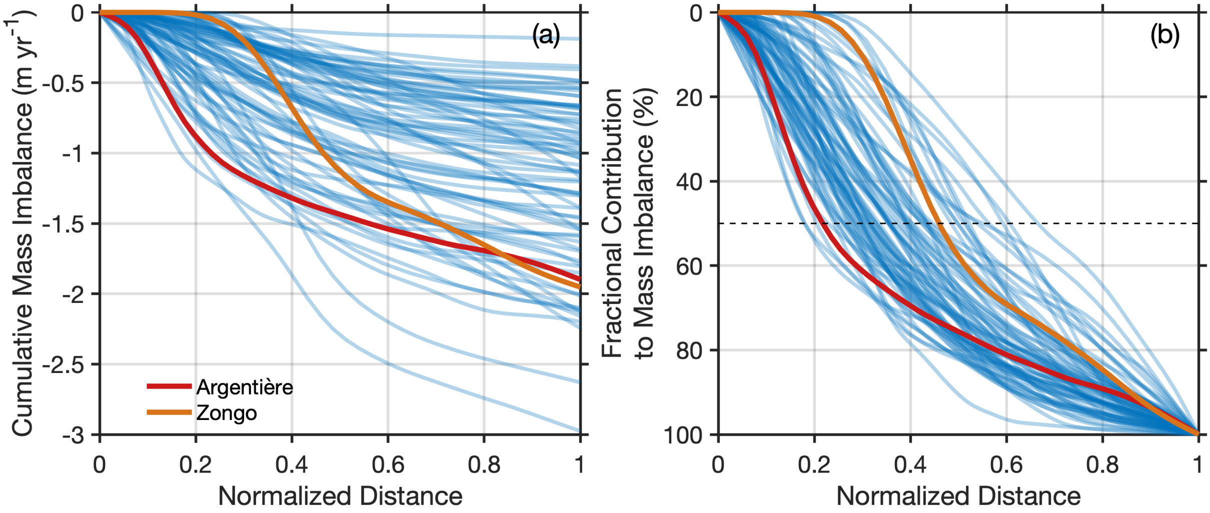

Figure 6. Cumulative mass imbalance for 75 glaciers spanning all major glacierized regions, shown as (a) absolute values (m yr^{-1}) and (b) fractional contribution (%). Each curve represents the integrated difference between accumulation and ablation from the glacier head (normalized distance = 0) to the terminus (normalized distance = 1). In panel (a), the terminal value reflects the glacier-wide mean mass imbalance. In panel (b), curves are normalized such that the terminus corresponds to 100% of the total imbalance, allowing comparison of spatial patterns across glaciers. The shape of each curve reflects the glacier's hypsometry (the distribution of glacier area with elevation). The intersection of each curve with the dashed horizontal line indicates the distance at which half of the mass loss has taken place, quantifying where along each glacier the imbalance is concentrated. Argentière glacier is highlighted in red, and Zongo glacier in orange.

4 Industrial-era changes in the context of the preindustrial millennium

We now contextualize the industrial-era mass-balance changes by comparing the observed changes to the range of natural climate variability from reconstructed climate histories of the last millennium. To do this, we draw on eleven unique, gridded reconstructions of near-surface air temperature over the last millennium (850-2000, Table A4) to estimate the envelope of natural mass-balance variability prior to industrialization. These reconstructions represent the best available estimates of preindustrial climate histories. 345

https://doi.org/10.5194/egusphere-2026-3164
Preprint. Discussion started: 23 June 2026

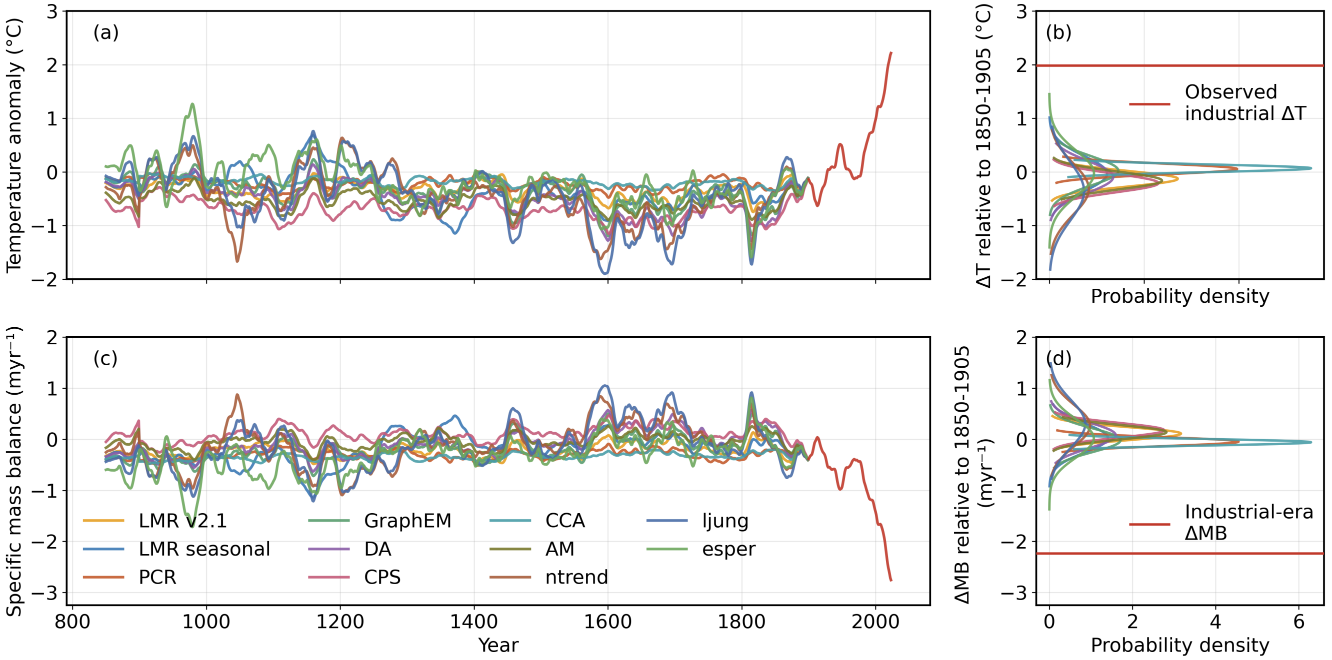

Figure 7. Last millennium temperature and mass-balance history at Argentière Glacier. (a) 30-year low-pass filtered seasonal temperature reconstruction from 11 last-millennium reanalyses (reconstruction details in Table A4), blended with Berkeley Earth observed temperatures (red) over the 1850-1900 period. Anomalies are shown with respect to the 1960-1990 period. (b) Distributions of last-millennium temperature for each reconstruction, computed with respect to the 1850-1905 base period, fit with a Gaussian; the red horizontal line marks the 15-year modern climate with respect to the 1850-1905 early-industrial mean (1.95 °C for Argentière, same as in Figure 1b). (c) Glacier-specific mass balance (m yr^{-1}) converted from reconstructed temperatures in panel (a), using the OGGM mass-balance profile for Argentière, and (d) Distribution of preindustrial (850-1850) mass-balance variability for each reconstruction; the red horizontal line indicates the modern (15-year mean) industrial-era mass-balance anomaly, all with respect to the early industrial (1850-1905) mean. (c) is a near mirror image of (a) because Argentière has a near-linear relationship between temperature and mass balance. This is not guaranteed for other geometries or mass-balance profiles.

Using Argentière as a case study again, we generate a continuous climate record from 850-2024 by combining the last-millennium reconstructions with the observed BE record. All records are referenced to a common 1960-1990 baseline. Because we are interested in climatological timescales, we apply a 30-year low-pass filter to the temperature anomalies before merging it with the equivalently filtered BE record, blending the two linearly over the 1850-1900 period such that all datasets converge smoothly onto the BE observed record by 1900. This yields a set of equally plausible climate histories, spanning 850 to present, each consistent with the modern observational record at this location and using equivalently defensible methodologies and paleoclimate proxy inputs (Figure 7a, Table A4).

https://doi.org/10.5194/egusphere-2026-3164
Preprint. Discussion started: 23 June 2026

The distribution of preindustrial temperature variability is computed for each reconstruction over the preindustrial period (850-1850), against which the observed industrial-era signal from Section 2.1 is compared. Our temperature histories are consistent with the well-known result that industrial-era warming lies well outside the range of temperatures of the preindustrial millennium (Fig. 7 a,b; Eyring et al., 2023). We now apply OGGM's calibrated mass-balance scheme using the same methodology described in Section 3.1 to convert the temperatures into mass-balance anomalies on the reference surface for Argentière. This provides a like-for-like comparison of the natural mass-balance variability over the preindustrial millennium, with that of the industrial-era warming. Figure 7b shows that the industrial-era mass-balance anomaly lies far outside the range of any fluctuations seen in the preceding millennium across all the proxy reconstructions. In IPCC language, it is *extremely likely* that industrial-era warming and mass balance lies outside the range experienced in the preindustrial millennium.

We extend this analysis to our global network of glaciers, focusing on the Last Millennium Reanalysis (LMR) seasonal reconstruction (Meng et al., 2025), since it is the only global product that allows us to compute melt-season rather than annual temperature anomalies. Figure 8 shows reference-surface mass balances for all 75 glaciers. Two things stand out. First is a small, overall positive mass balance in the few centuries preceding the industrial era, but with significant regional variability. Second is the magnitude and extraordinary coherence of mass loss over the industrial era. Moreover, for this climate reconstruction at least, there is no indication of any widespread natural warming preceding the industrial era that would contribute to an industrial-era retreat.

We define a mass-balance SNR for each glacier as the ratio of absolute attributable industrial-era mass-balance anomaly to the standard deviation of the detrended preindustrial millennium (850-1850) mass-balance timeseries. Across all of our sampled glaciers, we find industrial-era mass-balance anomalies are *extremely likely* (SNR>2) to lie outside the range of the preindustrial millennium (Fig. 9). These results, grounded in the best-available reconstructions of antecedent climate histories at each glacier site, provide an independent line of evidence that modern glacier mass loss is unprecedented within the context of the preindustrial millennium.

A few glaciers exhibit exceptionally high mass-balance SNRs (>20): Carstensz (Indonesia), Soler (South Andes) and Piedras Blancas (South Andes). The reasons for these extreme values differ across sites. At Carstensz, the glacier sits on a nearly flat summit plateau, meaning that even a modest temperature change produces a disproportionately large mass-balance anomaly. The flat geometry amplifies the sensitivity of the glacier, since a small upward shift of the ELA exposes a large area of the glacier to ablation. At Soler and Piedras Blancas, the elevated SNR arises from very small mass-balance variability at these sites. Although the local last-millennium temperature variability is comparable to other sites, when translated to mass balance using the local mass-balance profiles and glacier geometry, this temperature variability produces an order-of-magnitude smaller mass-balance variability than at most other sites. In other words, because these glaciers have a relatively shallow mass-balance profile, their mass balance is fairly insensitive to temperature fluctuations. At the same time, the large industrial-era temperature still produces a substantial mass-balance anomaly, driving the SNR to high values. These cases illustrate that the

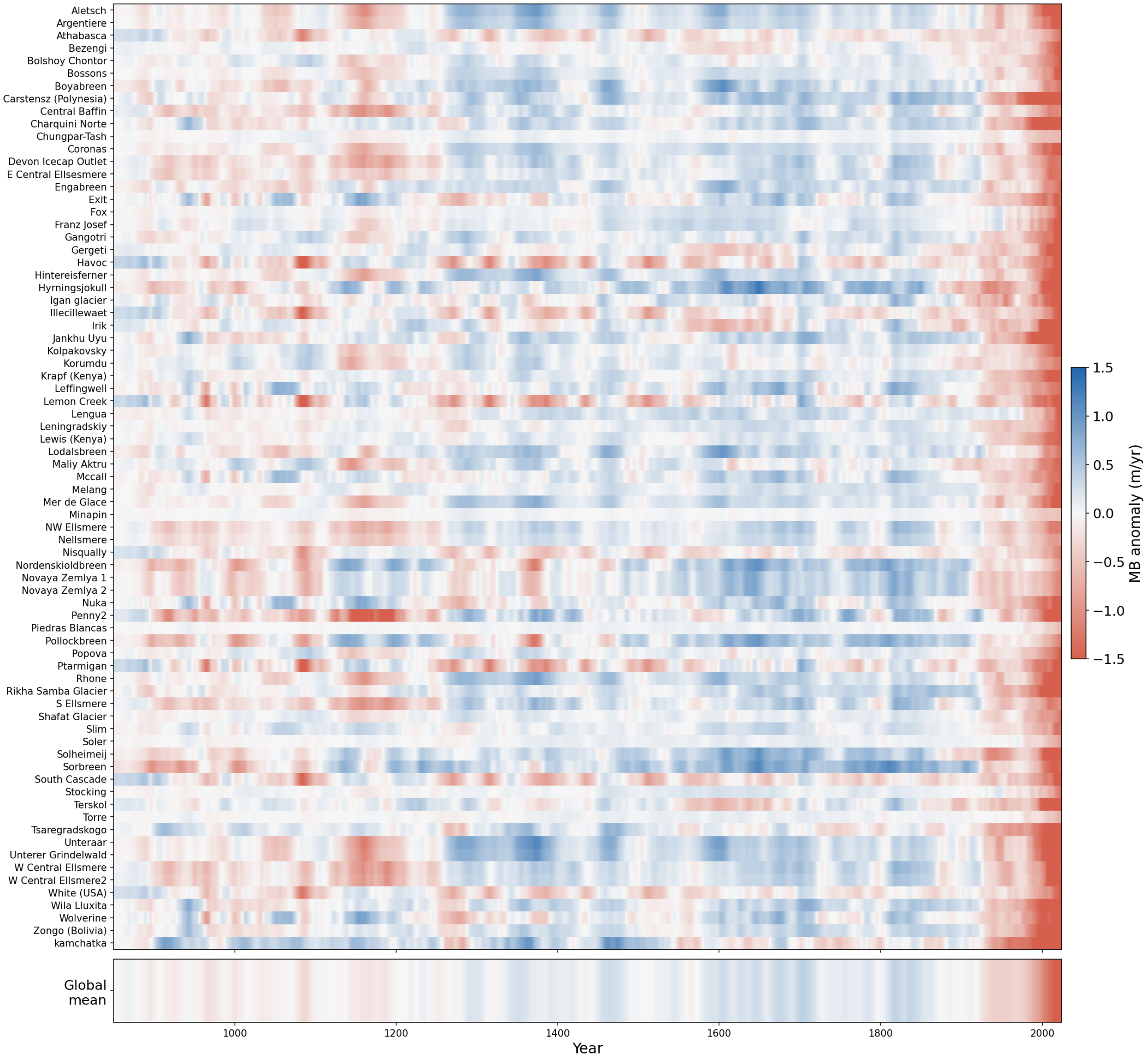

Figure 8. Annual reference-surface mass-balance anomaly for 75 glaciers spanning 850–2024 CE. Mass balance was estimated by applying the OGGM temperature-index scheme to a composite melt-season temperature record merging the Last Millennium Reanalysis (LMR) and Berkeley Earth observational datasets (dataset construction described in Section 4, and uses the same methodology converting Fig.7a to c). Each row represents an individual glacier, with anomalies computed relative to each glacier's long-term mean over the full 850–2024 period, such that positive (blue) and negative (red) values indicate above- and below-average mass-balance conditions respectively. The bottom strip shows the cross-glacier mean anomaly for each year.

https://doi.org/10.5194/egusphere-2026-3164
Preprint. Discussion started: 23 June 2026

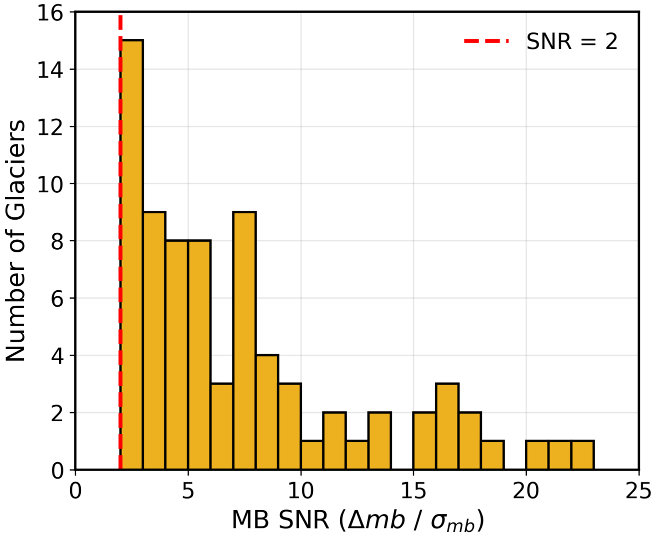

Figure 9. Distribution of mass-balance signal-to-noise (MB SNR) ratio calculated from the last millennium reconstruction seasonal dataset (Meng et al., 2025) for 75 global glaciers. The MB SNR is defined as the ratio of the attributable industrial-era mass-balance anomaly to the standard deviation of the detrended preindustrial (850-1850) mass-balance variability at each glacier. The dashed red line indicates the threshold SNR = 2, corresponding to a statement that the mass-balance signal is *extremely likely* to lie outside preindustrial variability.

mass-balance SNR is governed not only by the magnitude of the local climate signal, but also by the glacier-specific geometry and mass-balance sensitivity.

5 Summary and Discussion

We have extended standard climate-attribution methodologies to melt-season temperatures across all glacierized regions in the Randolph Glacier Inventory (except interior Antarctica and Greenland). By comparing observed industrial-era warming with a ∼200-member ensemble of natural-only GCM simulations, we find a central estimate of human-attributable warming ranges from 91–98% across all regions, with an area-weighted global average of 94% and a typical *likely* range of ±20% (Table 1). Notably, the upper end of the *likely* range exceeds 100% in all RGI regions, indicating that, absent human emissions, the climate might otherwise have been cooling. The attribution of industrial-era temperature change is robust across all RGI regions, with 16 out of 19 regions classified as *virtually certain* to be outside the natural range, and no region falling below the *extremely likely* category.

Converting these attributable temperature changes into attributable changes in ELA using local melt-season lapse rates, we find attributable ELA changes of hundreds of meters across all glacierized regions of the world. The greatest shifts occur in the

https://doi.org/10.5194/egusphere-2026-3164
Preprint. Discussion started: 23 June 2026

Canadian Arctic and the European Alps, where attributable ELA rise exceeds 300 m. Even the most modest regional signal in the Antarctic & Subantarctic, exceeds 100 m of change. These ELA changes are large relative to the typical vertical extent of glacier accumulation zones, implying significant impact on glacier net mass balance.

We transformed these climate analyses into glacier-relevant metrics by employing the concept of a glacier reference surface. By evaluating glacier mass balance over a fixed reference surface, we are able to directly characterize how the glacial environment has changed over the industrial-era in each catchment. The reference-surface approach allows us to circumvent the initialization and preindustrial-climate-forcing uncertainties that arise when modeling the dynamical glacier response. Actual glacier mass loss (i.e., what occurs on the evolving glacier surface), is simply a muted version of reference-surface mass loss. As such, all our assessments also apply to actual mass loss. Industrial-era temperature attribution is well established, and the application to glacier mass balance is a direct extension. The rising ELA and its impact on the reference surface follow directly from the attributed warming.

We evaluated 75 individual glaciers distributed across all RGI regions (except Antarctica and Greenland). When the industrial-era warming is applied to the reference glacier surfaces, roughly 70% of our glaciers experience at least a doubling of ablation, and a similar number of them experience more than a halving of accumulation. We also find that, for most glaciers, most of the change in reference-surface mass balance occurs in the upper half of the catchment, because ELAs have risen well into the preindustrial accumulation zones. The mass-balance SNR exceeds two at all but one site. Therefore, for our global glacier network, it is *extremely likely* that industrial-era mass-balance change exceeds what is possible in a natural climate. It is worth emphasizing that the reference-surface mass balance is not a measure of cumulative mass loss, but rather a direct measure of how the glacier environment has changed, making it cleanly relatable to the attributed temperature and ELA signals without the complication of dynamical buffering. Furthermore, the preindustrial reference surface plays an analagous role to the hist-nat simulations in that it can be seen as a counterfactual tool for isolating the anthropogenic signal. Our strong conclusion is that preindustrial glacier geometries simply cannot exist in their modern valley environments.

We have also evaluated the industrial-era mass-balance changes in the context of the reconstructed climate history of the past millennium. We show that even though there is considerable spread among different climate reconstructions at Argentière Glacier, all of which are considered equally plausible histories, the central estimate of attributable temperature and mass-balance changes remains well outside the preindustrial range (Fig. 7). Furthermore, we find no evidence that there was a significant antecedent climate imbalance at Argentière. Extending this analysis to all glaciers in our global network, we find industrial-era mass-balance anomalies are unprecedented within the past millennium (Fig. 8). This analysis provides another independent line of evidence, separate from the hist-nat counterfactual approach.

We have focused on the attribution of mass balance, highlighting Argentière as an example to lay out our methodology. As a final analysis, we apply the Roe and Baker (2014) three-stage glacier model to simulate the length and mass-balance re-

https://doi.org/10.5194/egusphere-2026-3164
Preprint. Discussion started: 23 June 2026

sponse of an Argentière-like glacier ($\tau = 30$ yr) to the full-millennium climate history. Driving the glacier model with the LMR seasonal reconstruction blended with the Berkeley Earth observed record, and including the same 205 hist-nat counterfactual simulations used throughout this study, we directly compare the simulated industrial-era length retreat under observed climate against the distribution of length changes that would have occurred under natural forcing alone (Fig.10). The glacier carries a small residual retreat tendency inherited from the end of the LIA, and the ensemble mean shows a modest industrial-era length decrease even under natural-only forcing, perhaps reflecting the reduced frequency of large volcanic eruptions over the twentieth century. Despite this inherited climate history, the observed retreat falls far outside the counterfactual envelope. We find that the central estimate of industrial-era retreat attributable to anthropogenic forcing is 85% of the observed retreat, with a *likely* range of ±20%. For the industrial-era cumulative mass loss (i.e., the integral of Fig. 10c since 1875), the central estimate is 90% anthropogenic with a *likely* range of ±20%. This is consistent with, and independently corroborates, the reference-surface mass-balance attribution results of this study. Full details of this simulation are provided in Appendix A.

Figure 10b is an example of a glacier-length simulation from a long (i.e., multi-century) climate scenario. As such we can be fully confident that the glacier length and state of disequilibrium at the start of the industrial era depend only on the antecedent climate history - they do not depend whatsoever on the initial condition at the start of the numerical integration (at 0 AD in this case). From the preindustrial reconstructions (Fig. 7), we do not see any climatic cause for a preindustrial glacier disequilibrium comparable to what develops over the industrial era. Other multi-century glacier simulations that we are aware of are consistent with this (e.g., Oerlemans, 2000; Parkes and Goosse, 2020; Huston et al., 2021; Roe et al., 2021). We identify a serious concern that numerical initial conditions do affect industrial-era glacier simulations that are initialized at 1850, the time that many industrial-era GCM runs become available. For such simulations, the initial glacier condition (including its state of disequilibrium) is determined only by the model calibration; it does not depend in any way on antecedent climate history, but it should. Numerical models suffer from numerical artifacts. Noise-induced drifts occur in the presence of mass balance and other nonlinearities (typically a retreat, e.g., Doughty, 2013); in any given climate state there is an envelope of natural variability of glacier locations in the valley that depends on an antecedent climate history, which can only be estimated for the preindustrial. Long numerical integrations and ensembles of plausible climate scenarios are needed to ensure results are not impacted by uncertainty in initial conditions. Two recent attribution studies initialize length simulations at 1850 (Marzeion et al., 2014a; Clauzel et al., 2023). Both exhibit significant initial disequilibria that contributes to substantial industrial-era retreat even under natural or control-climate scenarios. Such an initial disequilibrium needs to be shown to be consistent with antecedent climate history.

Putting our results into context, our attribution of industrial-era temperature changes and ELA estimates is fully consistent with the AR6 IPCC attribution statements on temperature (Eyring et al., 2023). Roe et al. (2017) demonstrated that glacier retreat amplifies the SNR of industrial-era instrumental records, and concluded that the observed retreats of ∼40 glaciers worldwide necessarily required a climate change. That particular study did not provide an attribution as to the cause of the required climate change, relying on that having been established in other work. Roe et al. (2021) used synthetic, reconstructed,

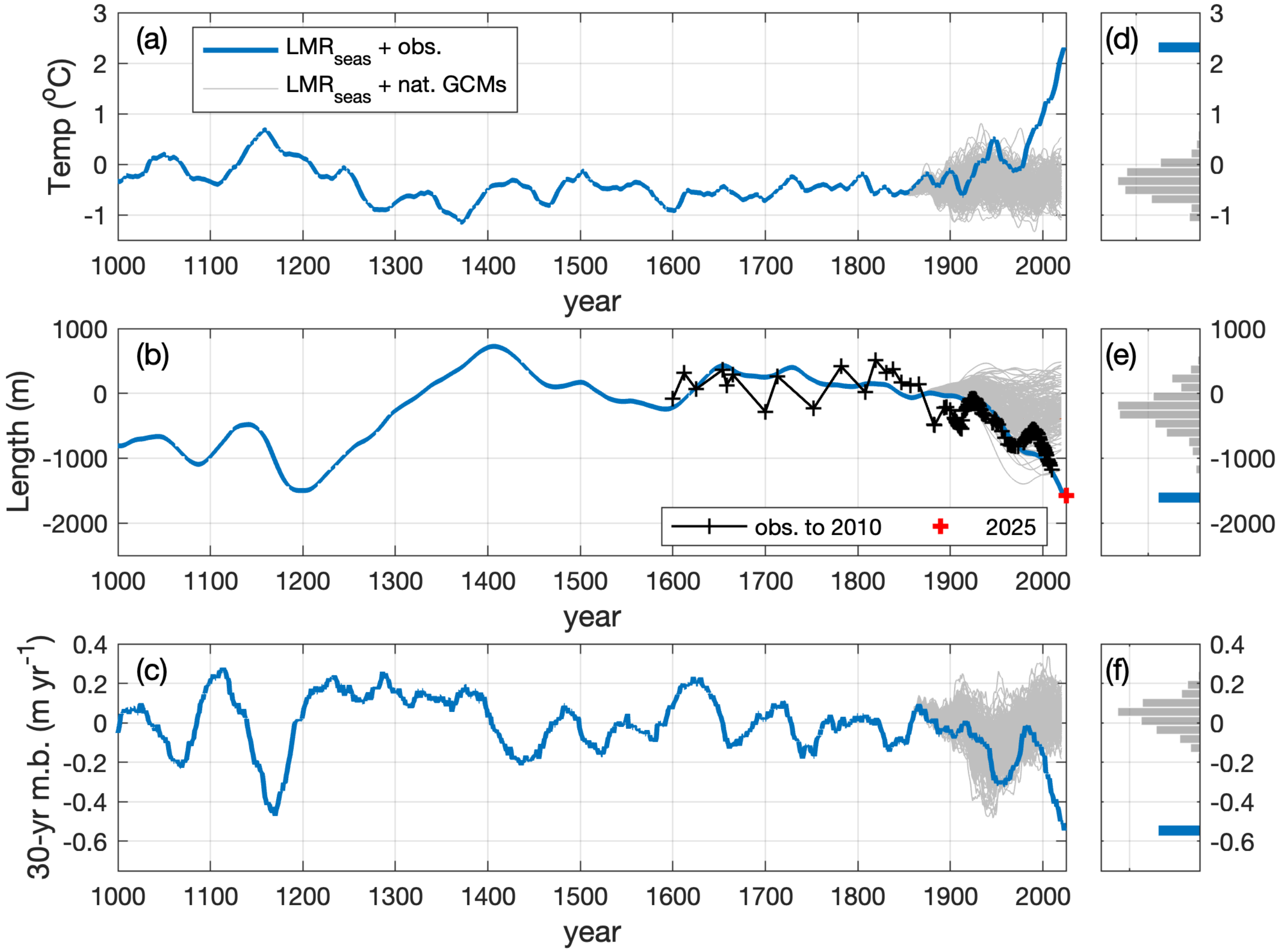

Figure 10. Three-stage glacier-model simulations for an Argentière-like glacier ($\tau = 30$ yr). (a) Melt-season temperature history from the LMR seasonal reconstruction, blended with BE observations (blue), and with $\sim$ 200 hist-nat climate-model simulations branching from 1850 (grey). (b) Simulated glacier-length anomaly relative to 1875 under BE (blue) and counterfactual ensemble (grey). Observed historical length changes at Argentière (Leclercq et al., 2014) are shown as black crosses (to 2010) and the 2025 observed length anomaly (estimated from Google Earth) as a red cross. (c) 30-year running-mean mass balance for the analagous cases. Right-hand panels (d,e,f) show histograms of the counterfactual ensemble (grey) and the final observed value (blue bar), illustrating the separation between the modern observed state and the envelope of natural variability.

and modeled past-millennium climates to conclude that, across a wide range of glacier response times, industrial-era mass loss was entirely due to anthropogenic forcing (central estimate). That study used the idealized geometry and the simple melt-factor ablation parameterization of the Roe and Baker (2014) three-stage model. This study here has built in some additional realism. We use realistic glacier-catchment geometries, a more sophisticated mass-balance scheme calibrated to each glacier, a large ensemble of ∼200 naturally forced GCMs, and eleven climate reconstructions of the past millennium to conclude that the industrial-era mass-balance changes for 75 glaciers worldwide lie far outside what can be accounted in a natural climate. Our results suggest that the anthropogenic impact on glacier mass balance is both larger and extends further back in time than the IPCC AR6 implies.

In future work, it could be useful to apply the modern mass-balance fields derived here to observed modern glacier profiles and evaluate whether the resulting thinning rates are consistent with geodetic observations (Hugonnet et al., 2021). While an upgrade in sophistication over prior work, the OGGM mass-balance scheme is still fairly simple. It would be possible to replay our analyses with a full surface-energy-balance mass-balance scheme that represents more meteorological factors (including precipitation and more seasonal resolution, following e.g., Rupper and Roe (2008)). We don't think that level of extra complexity would add value: the basic impact of increasing temperatures and rising snowlines on glacier mass balance is straightforward and clear.

Another direction, arguably more promising, for strengthening glacier attribution is the greater use of long preindustrial climate reconstructions, blended with the instrumental records to force glacier simulations. These would provide physically consistent and observation-based climate histories, distinct from the model-driven millennium simulations used in prior studies (e.g., Goosse et al., 2018). The example above using the Roe and Baker (2014) 3-stage model (Fig. 10) shows one such application, and could in theory be expanded to as many glacier regions as desired. This would allow a systematic evaluation of the impact of characteristics such as latitude, regional climate, and glacier geometry on a variety of glacier-response characteristics and their attribution confidence. Similarly, dynamical glacier models such as OGGM could be forced with long preindustrial millennium forcing, at local, regional or global scales. In contrast to models initialized in the mid-19th century, such experiments would allow realistic geometries to evolve naturally from their antecedent climate history, providing a physically consistent basis from which to evaluate industrial-era change. This approach would offer a means to evaluate the magnitude and characteristics of long-term natural variability, while largely avoiding the initialization concerns that have complicated prior attribution studies. We note, however, that the regional reconstructions carry their own uncertainties. The spread among reconstructions at any location reflects both methodological differences, and genuine uncertainty in the past climate.

Overall, our results provide a physically-grounded and geographically comprehensive glacier attribution analysis. The combination of realistic glacier geometries and mass-balance profiles from OGGM, combined with the reference-surface framework that removes the complications obscured by the dynamical glacier response, allows attribution to be performed at the individual glacier level across the globe for the first time. While the magnitude of the mass-balance responses varies considerably across glaciers, governed primarily by local glacier geometry rather than climatological setting, the direction of response is coherent and unambiguous. Across the global network we analyzed, it is at least *very likely*, and in the vast majority of cases *extremely likely* that industrial-era mass-balance changes lie outside the bounds of natural variability. We conclude it is *very likely* that anthropogenic climate change is the *primary driver* of industrial-era glacier mass loss.

Data availability. We use publicly available data sources. Berkeley Earth temperature data are available from Berkeley Earth (2026), CMIP5 data is available from the Earth System Grid Federation (2025) and CMIP6 was retrieved from the Pangeo Cloud Catalog (2025). Sources for the Last Millennium temperature reconstructions used in this study are outlined in Table A4, and are all publicly available. We use the Randolph Glacier Inventory Global Land Ice Measurements from Space (2026) and the Open Global Glacier Model Open Global Glacier Model (2026) for glacier geometry information.

Appendix A: Methods Details

A1 Climate Models

We collected a total of 205 hist-nat ensemble members from 28 (17 CMIP5 + 11 CMIP6) unique climate models (Table A1). Each ensemble member is considered a plausible counterfactual climate history, with the ensemble spread forming the population's natural variability. All climate models are regridded to the BE 1x1° grid. Global anomalies for BE and CMIP models are computed with respect to 1850-1900 except for Antarctica whose baseline climatology is 1960-1990 due to lack of data before 1956.

A2 3-stage glacier model

Figure 10 shows a calculation using the three-stage glacier model of Roe and Baker (2014). The model represents glacier dynamics through a third-order linear differential equation:

$$\left(\frac{d}{dt}+\frac{1}{\epsilon\tau}\right)^3 L' = \frac{1}{\epsilon^3\tau^2}\left(\beta P' - \alpha T'\right), \tag{A1}$$

where: L' is the length anomaly from some chosen mean state, T' is the melt-season temperature anomaly, P' is the annual precipitation anomaly (to approximate the accumulation anomaly); $\tau = -H/b_t$ is the glacier response time, H and b_t are the characteristic thickness and mass balance in the terminus zone; $\beta = A_{\mathrm{tot}}/wH$, A_{tot}, w are the total glacier area, and terminus-zone width; $\alpha = \mu A_{\mathrm{T}>0}/wH$, μ is a melt-season melt factor, and $A_{\mathrm{T}>0}$ is the melt area (Roe and Baker, 2014). For Argentière, we take $A_{\mathrm{tot}} = 14\times10^6\ \mathrm{m}^2$, $A_{\mathrm{T}>0} = 10\times10^6\ \mathrm{m}^2$, $w = 440\ \mathrm{m}$, $H = 250\ \mathrm{m}$, $b_t = -10\ \mathrm{m\ yr}^{-1}$ (e.g., Huybrechts et al., 1989; Maussion et al., 2019), and $\mu = 0{,}65\ \mathrm{m\ yr}^{-1}\ \mathrm{K}^{-1}$ giving, in round numbers, $\tau = 30$ yr, $\beta = 130$, and $\alpha = 60\ \mathrm{m\ yr}^{-1}\ \mathrm{K}^{-1}$.

A3 Last Millennium mass balance

The temperature histories in Figure 10a were created in the same way as for Figure 7 using the LMR seasonal reconstruction (Meng et al., 2025), with the ∼200 hist-nat simulations linearly blended to LMR between 1850 and 1900 and ensuring the same mean value over that period. White-noise precipitation was included with an interannual standard deviation of $0.2\ \mathrm{m\ yr}^{-1}$, consistent with gridded reanalysis data. Length anomalies are computed relative to the 1875 length for the three stage model and for the observed Leclercq et al. (2014) dataset. The 30-year running-mean mass balance shown in Figure 10c is the traditional mass balance calculated over the evolving glacier surface. The attributable fraction is a ratio: the numerator is the difference between the length anomaly driven by observed temperatures and the median length anomaly from the hist-nat temperatures; and the denominator is just length change driven by observed temperatures. In the same way, we can calculate an attributable fraction for the integrated mass loss.

Table A1. Summary of CMIP5 and CMIP6 hist-nat model ensembles used in this study.

Generation	Model	Period	Ensemble Members
CMIP5	ACCESS	1850–2020	3
	BCC	1850–2012	1
	CanESM	1850–2012	5
	CCSM4	1850–2005	4
	CESM1	1850–2005	3
	CNRM	1850–2012	6
	CSIRO	1850–2012	7
	FGOALS	1850–2009	3
	GFDL CM3	1860–2005	3
	GFDL ESM2M	1861–2005	1
	GISS-H	1850–2012	5
	GISS-R	1850–2012	5
	HadGEM	1860–2020	4
	IPSL HR	1850–2012	3
	IPSL LR	1850–2012	3
	MRI	1850–2005	1
	NorESM	1850–2012	1
CMIP5 Total			*58*
CMIP6	ACCESS CM2	1850–2020	3
	ACCESS ESM1	1850–2020	3
	BCC-CSM2-MR	1850–2020	3
	CanESM5	1850–2020	50
	CESM2	1850–2014	3
	FGOALS-g3	1850–2020	3
	GISS-E2-1-G	1850–2014	20
	HadGEM3-GC31	1850–2020	4
	MIROC6	1850–2020	50
	MRI-ESM2-0	1850–2020	5
	NorESM2-LM	1850–2020	3
CMIP6 Total			*147*
Combined Total			**205**

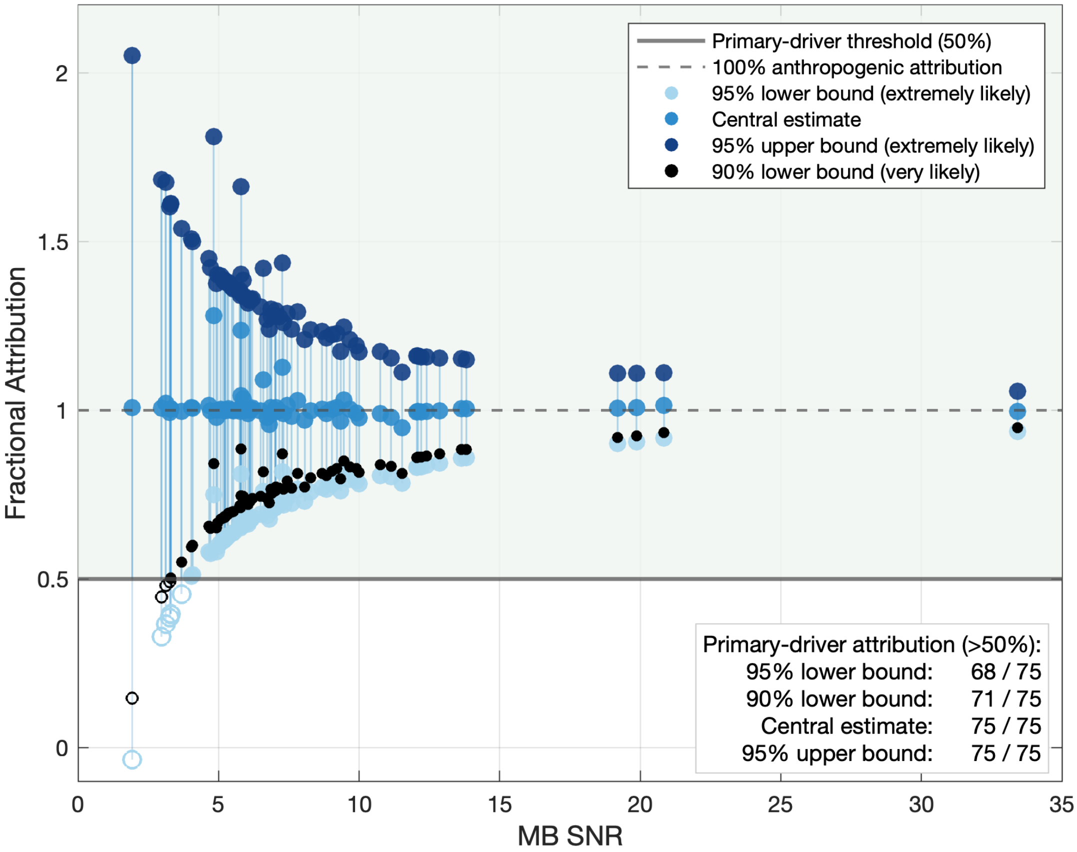

Figure A1. Fractional attribution of glacier mass-balance change to anthropogenic forcing for each of the 75 glaciers, plotted against glacier-specific mass-balance signal-to-noise ratio ($\mathrm{SNR} = \Delta\mathrm{MB}/\sigma_{\mathrm{MB}}$), where $\Delta\mathrm{MB}$ is the anthropogenically forced mass-balance change and σ_{MB} is the standard deviation of naturally forced changes in mass-balance estimated from the hist-nat ensemble. Fractional attribution is defined as $f = (\mathrm{MB}_{\mathrm{warmed}} - \mathrm{MB}_{\mathrm{baseline}})/\mathrm{MB}_{\mathrm{warmed}}$, where $\mathrm{MB}_{\mathrm{baseline}}$ represents the estimated mass balance in a counterfactual climate without anthropogenic warming and $\mathrm{MB}_{\mathrm{warmed}}$ represents the mass balance over the reference surface under a warmed climate. Attribution estimates are evaluated using baseline states of $\mu - 2\sigma_{MB}$, $\mu - 1.65\sigma_{MB}$, μ, and $\mu + 2\sigma_{MB}$ (where μ is the expected counterfactual mass balance from the hist-nat ensemble mean), corresponding respectively to the 95% lower bound, 90% lower bound (*very likely*), central estimate, and 95% upper bound. Light blue, black, medium blue, and dark blue markers denote these four attribution estimates. While the expected contribution of natural variability to ΔMB is near zero in the hist-nat ensemble, these uncertainty ranges account for the possibility that internal variability either enhanced or opposed the observed mass-balance trend. Lower SNR values indicate that natural variability is large relative to the forced signal, resulting in greater uncertainty in the inferred anthropogenic contribution. Filled circles indicate estimates exceeding the primary-driver threshold ($f > 0.5$), meaning that anthropogenic forcing accounts for more than half of the observed mass-balance change. Open circles indicate estimates below this threshold. The shaded region highlights $f > 0.5$, while the horizontal dashed line marks $f = 1.0$, corresponding to complete attribution of the observed mass loss to anthropogenic forcing. Values exceeding $f = 1$ indicate that, under the counterfactual baseline scenario, the glacier would have been expected to maintain neutral or positive mass balance in the absence of anthropogenic warming.

https://doi.org/10.5194/egusphere-2026-3164
Preprint. Discussion started: 23 June 2026

Table A2. IPCC probability terminology, and relationship to SNR assuming a Gaussian distribution (and using a conservative conversion to SNR). We adopt two-tailed probability thresholds throughout, which provides a conservative mapping between SNR and IPCC likelihood terminology.

SNR	Probability	IPCC Term
2.58	>99%	*Virtually Certain*
2.00	>95%	*Extremely Likely*
1.65	>90%	*Very Likely*
1.00	>68%	*Likely*

Table A3. Comprehensive glacier data for 75 glaciers. ΔT refers to the local melt-season attributable temperature change, as calculated using observed BerkeleyEarth temperatures (2010-2024) and CMIP counterfactuals. ΔMB is the implied change in mass balance, based on the local OGGM-derived mass-balance gradient. Acc. Ratio and Abl. Ratio refer to the accumulation and ablation scaling factors, (Acc_{now}/Acc_{LIA}, and Abl_{now}/Abl_{LIA}), respectively. L14 refers to Leclercq et al. (2014); P19 refers to Protin et al. (2019); N12 refers to Nussbaumer and Zumbühl (2012); R06 refers to Rabatel et al. (2006); D21 refers to Daiyrov and Narama (2021); D24 refers to Davies et al. (2024); R24 refers to Reinthaler and Paul (2024) EJ stands for Expert Judgment.

Glacier	RGI ID	Lat ($^{\circ}N$)	Lon ($^{\circ}E$)	ΔT (K)	ΔMB (m yr^{-1})	Accumulation Ratio	Ablation Ratio	ΔL resource	ΔL (m)
Aletsch	RGI60-11.01450	46.50	8.03	2.02	-2.098	0.39	2.03	L14	3206
Argentière	RGI60-11.03638	45.97	6.93	1.98	-1.899	0.31	2.09	L14 + P19	1696
Athabasca	RGI60-02.12441	52.20	-117.25	1.39	-0.780	0.46	1.76	L14	1596
Bezengi	RGI60-12.01252	43.05	43.07	1.96	-1.192	0.47	1.94	L14	2534
Bolshoy Chontor	RGI60-13.07952	41.97	77.90	1.25	-0.884	0.13	2.96	L14	1007
Bossons	RGI60-11.03646	45.87	6.78	1.98	-1.172	0.88	1.49	L14 + N12	1608
Boyabreen	RGI60-08.01103	61.30	6.46	1.36	-1.285	0.02	2.08	L14	1562
Carstensz	RGI60-16.01662	-4.10	137.17	1.33	-2.976	0.39	1.43	L14	2390
Central East Baffin	RGI60-04.00596	70.35	-71.09	1.49	-0.594	0.15	2.42	EJ	3000
Charquini Norte	RGI60-16.00548	-16.36	-68.12	1.33	-2.133	0.73	2.26	L14 + R06	1028
Chungpar-Tash	RGI60-14.20030	35.23	74.72	2.14	-0.687	0.73	1.65	L14	1200
Coronas	RGI60-11.03207	43.63	0.65	1.88	-1.388	0.00	7.00	L14	855
Devon Ice Cap	RGI60-03.02486	74.53	-81.62	1.16	-0.503	0.46	2.93	EJ	1500
East Central Ellesmere	RGI60-03.00166	79.78	-80.81	1.52	-0.538	0.10	2.57	EJ	2000
Engabreen	RGI60-08.01657	66.65	13.85	1.92	-1.581	0.02	4.15	L14	2371
Exit	RGI60-01.18087	60.17	-149.78	1.04	-0.908	0.27	2.08	L14	1875
Fox	RGI60-18.02375	-43.53	170.15	1.26	-1.592	0.57	1.45	L14	1750
Franz Josef	RGI60-18.02397	-43.50	170.22	1.26	-1.806	0.51	1.40	L14	2653
Gangotri	RGI60-15.06881	30.80	79.20	1.30	-1.392	0.67	1.56	L14	2110
Gergeti	RGI60-12.00709	42.65	44.57	1.99	-1.543	0.39	1.86	L14	1259
Havoc	RGI60-02.01461	50.52	-123.88	1.36	-1.128	0.28	2.15	L14	1208
Hintereisferner	RGI60-11.00897	46.80	10.77	2.08	-1.852	0.11	3.40	L14	2929
Hyrningsjokull	RGI60-06.00001	64.80	-23.77	0.76	-0.724	0.45	2.23	L14	1275
Illecillewaet	RGI60-02.03688	51.23	-117.47	1.40	-0.976	0.16	1.99	L14	1750
Igan	RGI60-10.05087	67.58	66.00	2.25	-1.519	0.00	6.50	EJ	1750

Continued on next page

https://doi.org/10.5194/egusphere-2026-3164
Preprint. Discussion started: 23 June 2026

Glacier	RGI ID	Lat ($^\circ N$)	Lon ($^\circ E$)	ΔT (K)	ΔMB (m yr^{-1})	Accumulation Ratio	Ablation Ratio	ΔL resource	ΔL (m)
Irik	RGI60-12.00730	43.33	42.50	1.98	-2.112	0.52	2.35	L14	1531
Jankhu Uyu	RGI60-16.00672	-16.05	-68.32	1.33	-2.631	0.01	4.42	L14	666
Kamchatka	RGI60-10.03529	56.62	159.61	1.48	-0.947	0.27	2.76	EJ	1500
Kolpakovsky	RGI60-13.07891	42.08	78.28	1.32	-1.003	0.26	2.60	L14	2178
Korumdu	RGI60-10.01729	50.13	87.68	1.00	-0.484	0.74	1.47	L14 + D21	689
Krapf	RGI60-16.01635	-0.13	37.32	1.34	-1.686	0.00	3.06	L14	551
Lemon Creek	RGI60-01.01104	58.38	-134.34	1.28	-1.303	0.05	2.85	D24	1500
Lengua	RGI60-17.04105	-52.80	-72.98	1.17	-2.244	0.77	1.80	L14	921
Leningradskiy	RGI60-09.00567	78.68	104.35	1.74	-0.757	0.00	5.05	EJ	2000
Lewis	RGI60-16.01638	-0.15	37.26	1.34	-1.697	0.00	2.37	L14	977
Leffingwell	RGI60-01.02169	69.29	-144.18	0.98	-0.405	0.34	2.05	L14	788
Lodalsbreen	RGI60-08.01131	61.78	7.24	1.96	-1.769	0.15	2.50	L14	3969
Maliyi Aktru	RGI60-10.01732	50.08	87.75	1.00	-0.535	0.45	1.56	L14	572
McCall	RGI60-01.02228	69.28	-143.83	0.99	-0.383	0.46	1.79	L14	831
Melang	RGI60-15.08054	28.45	99.73	1.62	-1.454	0.55	1.34	L14	1494
Mer de Glace	RGI60-11.03643	45.88	6.93	1.98	-1.796	0.49	1.63	L14	2435
Minapin	RGI60-14.04452	36.18	74.58	0.91	-0.188	0.87	1.28	L14	3000
N Ellsemere	RGI60-03.03735	82.60	-66.84	1.53	-0.557	0.35	2.34	EJ	2500
Nisqually	RGI60-02.14336	46.78	-121.75	1.58	-1.038	0.85	1.62	L14	2614
Nordenskioldbreen	RGI60-07.00570	78.70	17.18	1.92	-0.936	0.12	2.83	L14	2313
Novaya Zemlya 1	RGI60-09.00265	73.58	56.40	1.88	-0.829	0.00	3.63	R24 + EJ	2000
Novaya Zemlya 2	RGI60-09.00285	73.77	56.65	1.88	-0.795	0.00	4.44	R24 + EJ	2000
Nuka	RGI60-01.17995	59.66	-150.73	1.34	-1.032	0.24	2.26	L14	1326
NW Ellsemere	RGI60-03.03791	81.82	-86.23	1.51	-0.597	0.09	3.88	EJ	2000
Penny Ice Cap	RGI60-04.05654	67.58	-67.14	1.29	-0.864	0.00	3.88	EJ	2750
Piedras Blancas	RGI60-17.05091	-49.27	-72.97	1.26	-0.727	0.70	1.87	L14	1214
Pollockbreen	RGI60-07.00583	78.70	16.02	1.96	-1.085	0.02	4.18	L14	1202
Popova	RGI60-13.06740	41.99	77.93	1.25	-0.852	0.25	3.24	L14	1129
Ptarmigan	RGI60-01.01105	58.36	-134.37	1.28	-1.285	0.00	3.41	D24	1750
Rhone	RGI60-11.01238	46.62	8.40	2.02	-2.003	0.22	2.66	L14	2080
Rikha Samba	RGI60-15.04847	28.82	83.48	0.89	-1.631	0.50	1.79	EJ	2000

Continued on next page

Glacier	RGI ID	Lat ($^\circ N$)	Lon ($^\circ E$)	ΔT (K)	ΔMB (m yr^{-1})	Accumulation Ratio	Ablation Ratio	ΔL resource	ΔL (m)
Shafat	RGI60-14.16318	33.95	76.13	0.83	-0.489	0.72	1.39	EJ	1500
Slim	RGI60-01.08296	56.15	-159.15	1.28	-0.932	0.64	1.52	EJ	2000
Soler	RGI60-17.15844	-46.90	-73.18	1.29	-1.004	0.71	1.43	L14	1214
Solheimaj	RGI60-06.00340	63.58	-19.28	0.92	-1.136	0.56	1.52	L14	784
Sorbreen	RGI60-07.01568	71.03	-8.18	1.36	-1.135	0.59	2.10	L14	952
South Cascade	RGI60-02.18778	48.36	-121.06	1.47	-1.297	0.11	2.72	L14	4152
South Ellsemere	RGI60-03.01966	76.78	-88.01	1.50	-0.679	0.00	7.15	EJ	3000
Stocking	RGI60-18.01841	-43.67	170.07	1.26	-1.547	0.57	1.60	L14	622
Terskol	RGI60-12.00821	43.30	42.48	1.98	-2.015	0.55	2.26	L14	850
Torre	RGI60-17.05090	-49.35	-72.33	1.26	-0.673	0.77	1.95	L14	1225
Tsaregradskogo	RGI60-10.03162	65.24	146.07	1.37	-0.658	0.37	2.28	EJ	1500
U Grindewald	RGI60-11.01346*	46.58	8.07	2.02	-2.199	0.44	2.03	L14	1002
Unteraar	RGI60-11.01328	46.57	8.22	2.02	-2.159	0.34	2.42	L14	2268
W Central Ellsemere	RGI60-03.00948	78.98	-91.38	1.54	-0.667	0.13	4.17	EJ	2000
W Central Ellsemere 2	RGI60-03.00872	79.52	-89.26	1.57	-0.661	0.29	4.68	EJ	2000
White	RGI60-02.14009	47.87	-123.70	1.52	-1.465	0.14	2.75	L14	2530
Wila Lluxita	RGI60-16.00618	-16.05	-68.30	1.33	-2.121	0.00	7.61	L14	754
Wolverine	RGI60-01.09162	60.40	-148.92	1.26	-1.203	0.19	2.25	L14	1090
Zongo	RGI60-16.00543	-16.30	-68.14	1.32	-1.952	0.54	2.35	L14	815

Table A4. Last Millennium temperature reconstructions used in this study.

Reconstruction	Source	Details
LMR v2.1	Tardif et al. (2019)	Dynamical data assimilation, annual
LMR seasonal	Meng et al. (2025)	Dynamical data assimilation, seasonal
PCR	Neukom et al. (2019) & refs therein	Principal component regression, annual
GraphEM	Neukom et al. (2019) & refs therein	Gaussian graphical models, annual
DA	Neukom et al. (2019) & refs therein	Data assimilation, annual
CPS	Neukom et al. (2019) & refs therein	Composite plus scale, annual
CCA	Neukom et al. (2019) & refs therein	Canonical correlation analyis, annual
AM	Neukom et al. (2019) & refs therein	Analogue method, annual
ntrend	Anchukaitis et al. (2017)	Point-by-Point Regression, warm-season
ljung	Ljungqvist et al. (2019)	European warm-season temperature
esper	Esper et al. (2025)	Alpine Summer (JJAS) Alps Temperatures

Author contributions. Conceptualization: G.H.R.; Data Curation: M.B, G.H.R., Formal Analysis: M.B., G.H.R., J.E.C.; Writing – original draft: M.B., G.H.R., J.E.C.

Competing interests. The authors declare that they have no conflict of interest.

Acknowledgements. We thank Eric Steig for valuable discussions early on in this project. This work was funded by the National Science Foundation (NSF) EAR- 2314212 (M.B., G.H.R.) and start-up funds from University of Oregon (J.E.C.).

https://doi.org/10.5194/egusphere-2026-3164
Preprint. Discussion started: 23 June 2026

References

Allen, M. R. and Ingram, W. J.: Constraints on future changes in climate and the hydrologic cycle, Nature, 419, 224–232, 2002.

Anchukaitis, K. J., Wilson, R., Briffa, K. R., Büntgen, U., Cook, E. R., D'Arrigo, R., Davi, N., Esper, J., Frank, D., Gunnarson, B. E., et al.: Last millennium Northern Hemisphere summer temperatures from tree rings: Part II, spatially resolved reconstructions, Quaternary Science Reviews, 163, 1–22, 2017.

Atwood, A. R., Battisti, D., Wu, E., Frierson, D., and Sachs, J. P.: Data-model comparisons of tropical hydroclimate changes over the common era, Paleoceanography and Paleoclimatology, 36, e2020PA003 934, 2021.

Berkeley Earth: Berkeley Earth, Data overview, https://berkeleyearth.org/data/, 2026.

Bindoff, N. L., Stott, P. A., AchutaRao, K. M., Allen, M. R., Gillett, N., Gutzler, D., Hansingo, K., Hegerl, G., Hu, Y., Jain, S., et al.: Detection and attribution of climate change: from global to regional, Climate change 2013: the physical science basis, 2014.

Clauzel, L., Ménégoz, M., Gilbert, A., Gagliardini, O., Six, D., Gastineau, G., and Vincent, C.: Sensitivity of glaciers in the European Alps to anthropogenic atmospheric forcings: Case study of the Argentière Glacier, Geophysical Research Letters, 50, e2022GL100 363, 2023.

Cogley, J. G., Hock, R., Rasmussen, L., Arendt, A., Bauder, A., Braithwaite, R., Jansson, P., Kaser, G., Möller, M., Nicholson, L., et al.: Glossary of glacier mass balance and related terms, 2011.

Daiyrov, M. and Narama, C.: Formation, evolution, and drainage of short-lived glacial lakes in permafrost environments of the northern Teskey Range, Central Asia, Natural Hazards and Earth System Sciences, 21, 2245–2256, 2021.

Davies, B., McNabb, R., Bendle, J., Carrivick, J., Ely, J., Holt, T., Markle, B., McNeil, C., Nicholson, L., and Pelto, M.: Accelerating glacier volume loss on Juneau Icefield driven by hypsometry and melt-accelerating feedbacks, Nature Communications, 15, 5099, 2024.

Doughty, A.: Inferring past climate from moraine evidence using glacier modelling, Ph.D. thesis, Open Access Te Herenga Waka-Victoria University of Wellington, 2013.

Earth System Grid Federation: ESGF, https://metagrid.esgf-west.org/search, 2025.

Elsberg, D., Harrison, W., Echelmeyer, K., and Krimmel, R.: Quantifying the effects of climate and surface change on glacier mass balance, Journal of Glaciology, 47, 649–658, 2001.

Esper, J., Reinig, F., Torbenson, M., del Castillo, E. M., Kunz, M., Arzac, A., Carrer, M., Chen, F., Kadioglu, A. K., Kirdyanov, A. V., et al.: Pan-alpine summer temperatures since 742 CE, Dendrochronologia, 94, 126 432, 2025.

Eyring, V., Bony, S., Meehl, G. A., Senior, C. A., Stevens, B., Stouffer, R. J., and Taylor, K. E.: Overview of the Coupled Model Intercomparison Project Phase 6 (CMIP6) experimental design and organization, Geoscientific Model Development, 9, 1937–1958, 2016.

Eyring, V., Gillett, N. P., Achuta Rao, K. M., Barimalala, R., Barreiro Parrillo, M., Bellouin, N., Cassou, C., Durack, P. J., Kosaka, Y., McGregor, S., et al.: Human influence on the climate system (Chapter 3), IPCC 2021: Climate Change 2021: The Physical Science Basis. Contribution of Working Group I to the Sixth Assessment Report of the Intergovernmental Panel on Climate Change, pp. 423–552, 2023.

Forster, P., Storelvmo, T., Armour, K., Collins, W., Dufresne, J.-L., Frame, D., Lunt, D. J., Mauritsen, T., Palmer, M. D., Watanabe, M., Wild, M., and Zhang, H.: The Earth's Energy Budget, Climate Feedbacks, and Climate Sensitivity, in: Climate Change 2021: The Physical Science Basis, edited by Masson-Delmotte, V., Zhai, P., Pirani, A., Connors, S. L., Péan, C., Berger, S., Caud, N., Chen, Y., Goldfarb, L., Gomis, M. I., Huang, M., Leitzell, K., Lonnoy, E., Matthews, J. B. R., Maycock, T. K., Waterfield, T., Yelekçi, O., Yu, R., and Zhou, B., pp. 923–1054, Cambridge University Press, Cambridge, UK and New York, NY, USA, https://doi.org/10.1017/9781009157896.009, 2021.

Foster, G. and Rahmstorf, S.: Global warming has accelerated significantly, Geophysical Research Letters, 53, e2025GL118 804, 2026.

Gillett, N. P., Arora, V. K., Matthews, D., and Allen, M. R.: Constraining the ratio of global warming to cumulative CO 2 emissions using CMIP5 simulations, Journal of Climate, 26, 6844–6858, 2013.

Gillett, N. P., Kirchmeier-Young, M., Ribes, A., Shiogama, H., Hegerl, G. C., Knutti, R., Gastineau, G., John, J. G., Li, L., Nazarenko, L., et al.: Constraining human contributions to observed warming since the pre-industrial period, Nature Climate Change, 11, 207–212, 2021.

GLIMS and NSIDC: Global Land Ice Measurements from Space Glacier Database, https://doi.org/10.7265/N5V98602, updated 2018. Compiled and made available by the international GLIMS community and the National Snow and Ice Data Center, Boulder CO, U.S.A., 2005.

Global Land Ice Measurements from Space: Randolph Glacier Inventory, https://www.glims.org/RGI/, 2026.

Goosse, H., Barriat, P.-Y., Dalaiden, Q., Klein, F., Marzeion, B., Maussion, F., Pelucchi, P., and Vlug, A.: Testing the consistency between changes in simulated climate and Alpine glacier length over the past millennium, Climate of the Past, 14, 1119–1133, 2018.

Grove, J. M.: Little Ice Ages Vol2 Ed2, Routledge, 2013.

Harrison, W., Elsberg, D., Cox, L., and March, R.: Different mass balances for climatic and hydrologic applications, Journal of Glaciology, 51, 176–176, 2005.

Hegerl, G. C., Hoegh-Guldberg, O., Casassa, G., Hoerling, M., Kovats, S., Parmesan, C., Pierce, D., and Stott, P.: Good practice guidance paper on detection and attribution related to anthropogenic climate change, 2010.

Held, I. M. and Soden, B. J.: Robust responses of the hydrological cycle to global warming, Journal of climate, 19, 5686–5699, 2006.

Hersbach, H., Bell, B., Berrisford, P., Hirahara, S., Horányi, A., Muñoz-Sabater, J., Nicolas, J., Peubey, C., Radu, R., Schepers, D., et al.: The ERA5 global reanalysis, Quarterly journal of the royal meteorological society, 146, 1999–2049, 2020.

Hugonnet, R., McNabb, R., Berthier, E., Menounos, B., Nuth, C., Girod, L., Farinotti, D., Huss, M., Dussaillant, I., Brun, F., et al.: Accelerated global glacier mass loss in the early twenty-first century, Nature, 592, 726–731, 2021.

Huss, M., Hock, R., Bauder, A., and Funk, M.: Conventional versus reference-surface mass balance, Journal of Glaciology, 58, 278–286, 2012.

Huston, A., Siler, N., Roe, G. H., Pettit, E., and Steiger, N. J.: Understanding drivers of glacier-length variability over the last millennium, The Cryosphere, 15, 1645–1662, 2021.

Huybrechts, P., De Nooze, P., and Decleir, H.: Numerical modelling of Glacier d'Argentière and its historic front variations, in: Glacier Fluctuations and Climatic Change: Proceedings of the Symposium on Glacier Fluctuations and Climatic Change, held in Amsterdam, 1–5 June 1987, pp. 373–389, Springer, 1989.

Jenkins, S., Povey, A., Gettelman, A., Grainger, R., Stier, P., and Allen, M.: Is anthropogenic global warming accelerating?, Journal of Climate, 35, 7873–7890, 2022.

Larocca, L. J., Lea, J. M., Erb, M. P., McKay, N. P., Phillips, M., Lamantia, K. A., and Kaufman, D. S.: Arctic glacier snowline altitudes rise 150 m over the last 4 decades, The Cryosphere, 18, 3591–3611, 2024.

Leclercq, P. W., Oerlemans, J., Basagic, H. J., Bushueva, I., Cook, A., and Le Bris, R.: A data set of worldwide glacier length fluctuations, The Cryosphere, 8, 659–672, 2014.

Ljungqvist, F. C., Seim, A., Krusic, P. J., González-Rouco, J. F., Werner, J. P., Cook, E. R., Zorita, E., Luterbacher, J., Xoplaki, E., Destouni, G., et al.: European warm-season temperature and hydroclimate since 850 CE, Environmental Research Letters, 14, 084 015, 2019.

Marzeion, B., Hofer, M., Jarosch, A., Kaser, G., and Mölg, T.: A minimal model for reconstructing interannual mass balance variability of glaciers in the European Alps, The Cryosphere, 6, 71–84, 2012.

Marzeion, B., Cogley, J. G., Richter, K., and Parkes, D.: Attribution of global glacier mass loss to anthropogenic and natural causes, Science, 345, 919–921, 2014a.

Marzeion, B., Jarosch, A., and Gregory, J. M.: Feedbacks and mechanisms affecting the global sensitivity of glaciers to climate change, The Cryosphere, 8, 59–71, 2014b.

Marzeion, B., Kaser, G., Maussion, F., and Champollion, N.: Limited influence of climate change mitigation on short-term glacier mass loss, Nature Climate Change, 8, 305–308, 2018.

Masson-Delmotte, V., Zhai, P., Pirani, A., Connors, S. L., Péan, C., Berger, S., Caud, N., Chen, Y., Goldfarb, L., Gomis, M. I., et al.: Climate change 2021: the physical science basis, Contribution of working group I to the sixth assessment report of the intergovernmental panel on climate change, 2, 2391, 2021.

Maussion, F., Butenko, A., Champollion, N., Dusch, M., Eis, J., Fourteau, K., Gregor, P., Jarosch, A. H., Landmann, J., Oesterle, F., et al.: The open global glacier model (OGGM) v1. 1, Geoscientific Model Development, 12, 909–931, 2019.

Meng, Z., Hakim, G. J., and Steig, E. J.: Coupled seasonal data assimilation of sea ice, ocean, and atmospheric dynamics over the last millennium, Journal of Climate, 38, 7229–7247, 2025.

Minière, A., von Schuckmann, K., Sallée, J.-B., and Vogt, L.: Robust acceleration of Earth system heating observed over the past six decades, Scientific Reports, 13, 22 975, 2023.

Neukom, R., Steiger, N., Gómez-Navarro, J. J., Wang, J., and Werner, J. P.: No evidence for globally coherent warm and cold periods over the preindustrial Common Era, Nature, 571, 550–554, 2019.

Nussbaumer, S. U. and Zumbühl, H. J.: The Little Ice Age history of the Glacier des Bossons (Mont Blanc massif, France): a new high-resolution glacier length curve based on historical documents, Climatic Change, 111, 301–334, 2012.

Oerlemans, J.: An attempt to simulate historic front variations of Nigardsbreen, Norway, Theoretical and applied climatology, 37, 126–135, 1986.

Oerlemans, J.: Holocene glacier fluctuations: is the current rate of retreat exceptional?, Annals of Glaciology, 31, 39–44, 2000.

Ohmura, A. and Boettcher, M.: On the shift of glacier equilibrium line altitude (ELA) under the changing climate, Water, 14, 2821, 2022.

Open Global Glacier Model: OGGM, https://www.glims.org/RGI/, 2026.

Pangeo Cloud Catalog: Accessing data in the cloud, https://pangeo-data.github.io/pangeo-cmip6-cloud/pangeo_catalog.html, 2025.

Parkes, D. and Goosse, H.: Modelling regional glacier length changes over the last millennium using the Open Global Glacier Model, The Cryosphere, 14, 3135–3153, 2020.

Paul, F.: The influence of changes in glacier extent and surface elevation on modeled mass balance, The Cryosphere, 4, 569–581, 2010.

Protin, M., Schimmelpfennig, I., Mugnier, J.-L., Ravanel, L., Le Roy, M., Deline, P., Favier, V., Buoncristiani, J.-F., Aumaître, G., Bourlès, D. L., et al.: Climatic reconstruction for the Younger Dryas/Early Holocene transition and the Little Ice Age based on paleo-extents of Argentière glacier (French Alps), Quaternary Science Reviews, 221, 105 863, 2019.

Rabatel, A., Machaca, A., Francou, B., and Jomelli, V.: Glacier recession on Cerro Charquini (16 S), Bolivia, since the maximum of the Little Ice Age (17th century), Journal of Glaciology, 52, 110–118, 2006.

Rabatel, A., Letréguilly, A., Dedieu, J.-P., and Eckert, N.: Changes in glacier equilibrium-line altitude in the western Alps from 1984 to 2010: evaluation by remote sensing and modeling of the morpho-topographic and climate controls, The Cryosphere, 7, 1455–1471, 2013.

Rabatel, A., Sanchez, O., Vincent, C., and Six, D.: Estimation of glacier thickness from surface mass balance and ice flow velocities: a case study on Argentière Glacier, France, Frontiers in Earth Science, 6, 112, 2018.

https://doi.org/10.5194/egusphere-2026-3164
Preprint. Discussion started: 23 June 2026

Reinthaler, J. and Paul, F.: Assessment of methods for reconstructing Little Ice Age glacier surfaces on the examples of Novaya Zemlya and the Swiss Alps, Geomorphology, 461, 109 321, 2024.

Ribes, A., Qasmi, S., and Gillett, N. P.: Making climate projections conditional on historical observations, Science Advances, 7, eabc0671, 2021.

Roe, G. H.: What do glaciers tell us about climate variability and climate change?, Journal of Glaciology, 57, 567–578, 2011.

Roe, G. H. and Baker, M. B.: Glacier response to climate perturbations: an accurate linear geometric model, Journal of Glaciology, 60, 670–684, 2014.

Roe, G. H., Baker, M. B., and Herla, F.: Centennial glacier retreat as categorical evidence of regional climate change, Nature Geoscience, 10, 95–99, 2017.

Roe, G. H., Christian, J. E., and Marzeion, B.: On the attribution of industrial-era glacier mass loss to anthropogenic climate change, The Cryosphere, 15, 1889–1905, 2021.

Rohde, R. A. and Hausfather, Z.: The Berkeley Earth land/ocean temperature record, Earth System Science Data Discussions, 2020, 1–16, 2020.

Rupper, S. and Roe, G.: Glacier changes and regional climate: a mass and energy balance approach, Journal of Climate, 21, 5384–5401, 2008.

Solomina, O. N., Bradley, R. S., Jomelli, V., Geirsdottir, A., Kaufman, D. S., Koch, J., McKay, N. P., Masiokas, M., Miller, G., Nesje, A., et al.: Glacier fluctuations during the past 2000 years, Quaternary Science Reviews, 149, 61–90, 2016.

Tardif, R., Hakim, G. J., Perkins, W. A., Horlick, K. A., Erb, M. P., Emile-Geay, J., Anderson, D. M., Steig, E. J., and Noone, D.: Last Millennium Reanalysis with an expanded proxy database and seasonal proxy modeling, Climate of the Past, 15, 1251–1273, 2019.

Taylor, K. E., Stouffer, R. J., and Meehl, G. A.: An overview of CMIP5 and the experiment design, Bulletin of the American meteorological Society, 93, 485–498, 2012.